CrossMark

# Microstability of $\beta \sim 1$ tokamak equilibria

**Rahul Gaur** [1],†, **Ian G. Abel** [1], **David Dickinson** [2] **and**
**William D. Dorland** [1,3]

[1]Institute for Research in Electronics and Applied Physics, University of Maryland, College Park,
MD 20740, USA

[2]Department of Physics, University of York, Heslington, York YO10 5DD, UK

[3]Department of Physics, University of Maryland, College Park, MD 20740, USA

High-power-density tokamaks offer a potential solution to design cost-effective fusion
devices. One way to achieve high power density is to operate at a high $\beta$ value
(the ratio of thermal to magnetic pressure), i.e. $\beta \sim 1$. However, a $\beta \sim 1$ state may
be unstable to various pressure- and current-driven instabilities or have unfavourable
microstability properties. To explore these possibilities, we generate $\beta \sim 1$ equilibria and
investigate their stability. First, we demonstrate the generation of high-$\beta$ equilibria with
the computer code VMEC. We then analyse these equilibria to determine their stability
against the infinite-$n$ ideal-ballooning mode. We follow that by engaging in a detailed
microstability study using the GS2 code, beginning with assessments of electrostatic
ion-temperature-gradient and trapped election mode instabilities. We observe interesting
behaviour for the high-$\beta$ equilibria – stabilization of these modes through two distinct
mechanisms – large negative local shear and reversal of electron precession drift. Finally,
we perform electromagnetic gyrokinetic simulations and observe enhanced stability in
the outer core of high-$\beta$ equilibria and absence of kinetic ballooning modes in the
negative-triangularity, high-$\beta$ equilibria. The enhanced outer-core stability of high-$\beta$
equilibria is different from their lower-$\beta$ counterparts and offers an alternative, potentially
favourable regime of tokamak operation.

**Key words:** fusion plasma, plasma simulation, plasma instabilities

---

## 1. Introduction

The most advanced fusion reactor designs are currently based on the tokamak concept.
These tokamak designs have historically led to large volume, large capital cost, plants such
as ITER (Shimada *et al.* 2007) and EU-DEMO (Federici *et al.* 2014). Improvements in
these designs could be achieved by operating at high power density, with reduced plasma
volume (Menard *et al.* 2022).

For a fixed magnetic field strength, the power density of a tokamak $P$ scales as $\beta^2$, where
$\beta$ is the ratio of the plasma pressure to the magnetic pressure. Present-day tokamaks are

† Email address for correspondence: rgaur@umd.edu

low-$\beta$ devices. The achievable $\beta$ is typically limited by plasma instabilities. These can lead to disruptions or large turbulent transport. The higher $\beta$ is, the higher the pressure and current are, and therefore the larger the free energy available to drive these instabilities is. If these problems could be overcome, high-$\beta$ operation could be an attractive choice for future high-power-density (Menard *et al.* 2022) devices.

The high-beta, $\beta \sim 1$, regime has been explored previously in the context of asymptotic magnetohydrodynamic (MHD) equilibria by solving the Grad–Shafranov equation in the limit $\epsilon/(\beta q^2) \ll 1$ (Hsu, Artun & Cowley 1996) where $\epsilon$ is the aspect ratio of the tokamak and $q$ is the safety factor defined in (**??**):. There have also been experimental explorations (Sykes *et al.* 2000; Gates & NSTX National Research Team 2003) of high-$\beta$ operation of the MAST and START tokamaks. There have only been a few studies (Chance *et al.* 1990; Hurricane, Chandran & Cowley 2000) that investigated the process of accessing these states while maintaining ideal-MHD stability; even fewer studies that study the microstability properties of $\beta \sim 1$ equilibria in detail (Wilson *et al.* 2004). Therefore, a detailed numerical analysis of these types of equilibria is required.

To that end, we generate a set of high-$\beta$ equilibria and study their susceptibility to local MHD and gyrokinetic instabilities. In context of local MHD, we study stability of these equilibria to the infinite-$n$, ideal-ballooning mode. Then we perform linear gyrokinetic analyses against various electrostatic and electromagnetic modes of instability in these equilibria. These modes are known to cause significant heat and particle transport in existing devices (White *et al.* 2013; Creely *et al.* 2017)

The remainder of this paper is divided as follows: in § 2, we briefly describe the fundamentals of an axisymmetric equilibrium. In § 2.1, we obtain numerical equilibria using the VMEC code (Hirshman & Whitson 1983). We describe and plot the equilibria for three different beta values: low-$\beta$ ($\beta \sim 0.01$), intermediate-$\beta$ ($\beta \sim 0.1$) and high-$\beta$ ($\beta \sim 1$) and two different triangularity values. In § 3, we introduce the technique devised by Greene & Chance (1981) to vary gradients of a local equilibria. We then use this to analyse the susceptibility of the chosen local equilibria to the ideal-ballooning instability and explain our observations. After ensuring ideal-ballooning stability for our high-$\beta$ equilibria, in § 4, we briefly explain the linear, collisionless, gyrokinetic model and process for analysing kinetic stability of local equilibria using the gyrokinetic code GS2. In § 5, we solve the gyrokinetic model for electrostatic fluctuations with adiabatic electrons and use the same techniques that we used in § 3 to scan the growth rates of all the local equilibria with respect to the temperature gradient. In § 6, we solve the gyrokinetic model for electrostatic fluctuations after relaxing the assumption of adiabatic electrons and use the same techniques as § 3 to scan the growth rates of all the local equilibria with respect to the density gradient. In § 7, we study the stability of local equilibria at their nominal gradients to electromagnetic fluctuations by solving the full gyrokinetic model and explain the advantages of negative-triangularity, high-$\beta$ equilibria. Finally in § 8, we summarize our work and discuss the directions in which it can be extended.

## 2. Generating axisymmetric $\beta \sim 1$ equilibria

In this section, we will start with the general form of a divergence-free magnetic field, simplify it for an axisymmetric configuration and using the simplified form, obtain an explicit form of the steady-state momentum equation – the Grad–Shafranov equation. In § 2.1, we briefly explain how VMEC works and provide details for the equilibria generated for this work.

A divergence-free magnetic field $\boldsymbol{B}$ can be written in the Clebsch form (D'haeseleer *et al.* 2012)

$$\boldsymbol{B} = \boldsymbol{\nabla}\alpha \times \boldsymbol{\nabla}\psi. \tag{2.1}$$

We shall restrict our attention to solutions whose magnetic field lines lie on closed nested toroidal surfaces, known as flux surfaces. We label the flux surfaces by their enclosed poloidal flux $\psi$. On each flux surface, the line of constant $\alpha$, the field-line label, gives us the path of the magnetic field line.

We will use the right-handed, cylindrical coordinate system $(R, \phi, Z)$ where $R$ and $Z$ are the radial and vertical distance from the origin and $\phi$ is the azimuthal angle about the symmetry axis. We also define a curvilinear coordinate system $(\psi, \phi, \theta)$ with $\psi$ being the flux surface label, $\phi$ being the cylindrical azimuthal angle and $\theta$ being the 'straight-field-line' poloidal angle (D'haeseleer *et al.* 2012) such that $\alpha = \phi - q(\psi)\theta$ where

$$q(\psi) \equiv \frac{\mathrm{d}\chi}{\mathrm{d}\psi} = \frac{1}{2\pi} \oint \mathrm{d}\theta \frac{\boldsymbol{B} \cdot \boldsymbol{\nabla}\phi}{\boldsymbol{B} \cdot \boldsymbol{\nabla}\theta} = \frac{\boldsymbol{B} \cdot \boldsymbol{\nabla}\phi}{\boldsymbol{B} \cdot \boldsymbol{\nabla}\theta}, \tag{2.2}$$

is the safety factor, $\chi$ is the enclosed toroidal flux, and the line integral is over $\theta \in [0, 2\pi]$. The relation for $q(\psi)$ is consistent with the definition of $\alpha = \phi - q\theta$ as can be seen by substituting $\alpha$ into (2.1), obtaining

$$\boldsymbol{B} = \boldsymbol{\nabla}\phi \times \boldsymbol{\nabla}\psi - q\boldsymbol{\nabla}\theta \times \boldsymbol{\nabla}\psi, \tag{2.3}$$

and noting that (2.3) satisfies (2.2). For an axisymmetric $\boldsymbol{B}$, (2.3) can be reduced further, to

$$\boldsymbol{B} = \boldsymbol{\nabla}\phi \times \boldsymbol{\nabla}\psi + F\boldsymbol{\nabla}\phi. \tag{2.4}$$

Here, $F = F(\psi, \theta)$. To generate an MHD equilibrium one has to solve the steady-state, ideal-MHD force balance equation (Freidberg 2014) which, in SI units, is

$$\boldsymbol{\nabla}p = \frac{(\boldsymbol{\nabla} \times \boldsymbol{B}) \times \boldsymbol{B}}{\mu_0} = \frac{\boldsymbol{B} \cdot \boldsymbol{\nabla}\boldsymbol{B}}{\mu_0} - \boldsymbol{\nabla}\left(\frac{B^2}{2\mu_0}\right), \tag{2.5}$$

where $p$ is the plasma pressure and $\mu_0$ is the vacuum magnetic permeability. For an axisymmetric system, we can substitute the form of $\boldsymbol{B}$ from (2.4) and choose the toroidal component of (2.5) to get $\boldsymbol{B} \cdot \boldsymbol{\nabla}F = 0$ which implies $F = F(\psi)$. Upon choosing the radial component, we obtain the Grad–Shafranov (Shafranov 1957; Grad & Rubin 1958) equation

$$\boldsymbol{\Delta}^*\psi \equiv R^2\boldsymbol{\nabla} \cdot \left(\frac{\boldsymbol{\nabla}\psi}{R^2}\right) = -\mu_0 R^2 \frac{\mathrm{d}p}{\mathrm{d}\psi} - F\frac{\mathrm{d}F}{\mathrm{d}\psi}. \tag{2.6}$$

The Grad–Shafranov equation is a nonlinear equation for the poloidal flux $\psi(R, Z)$ that depends on the pressure $p(\psi)$ and current $F(\psi)$ profiles. As discussed in the introduction, for a fixed field strength $B$, the fusion power output $P$ of a tokamak scales as $\beta^2$ – $\beta \equiv p/(B^2/(2\mu_0))$ is the ratio of plasma pressure to magnetic pressure – which makes high-$\beta$ operation an attractive concept. Therefore, our objective is to analyse the stability of equilibria that have $\beta \sim 1$.

To create high-$\beta$ equilibria, one may start with analytical solutions of the Grad–Shafranov equation. The most general analytical solution in the $\beta \sim 1$ limit was obtained by Hsu, Artun and Cowley (Hsu *et al.* 1996). However, these analytical $\beta \sim 1$ equilibria are unfit for our study as the geometric quantities required for a local stability analysis can be discontinuous and deviate significantly from the exact numerical solution. We briefly

explain the analytical procedure used to calculate such equilibria and their limitations in Appendix A. To avoid these issues, we will use the equilibrium solver VMEC to generate high-$\beta$, axisymmetric equilibria in the next section.

### 2.1. *Numerical equilibria*

We generate equilibria numerically using the three-dimensional (3-D) equilibrium code VMEC (Hirshman & Whitson 1983). VMEC works by minimizing the integral

$$W = \int \left( \frac{p}{\gamma - 1} + \frac{B^2}{2\mu_0} \right) \mathrm{d}V, \tag{2.7}$$

subject to multiple constraints, which for axisymmetric equilibria is equivalent to solving the Grad–Shafranov equation (Kruskal & Kulsrud 1958). For our study, VMEC takes the shape of the boundary surface along with the global radial pressure $p(s)$ and safety factor $q(s)$ or enclosed toroidal current $G(s)$ as a function of the normalized toroidal flux $s$. It then creates flux surfaces to minimize the integral in (2.7) on each surface for a fixed $p$ and $q$ (or $G$) subject to various constraints. We choose the safety factor instead of toroidal current as it varies slowly (Abel & Cowley 2013) compared with the plasma currents in the limit of small electron-to-ion mass ratio.

   In the following paragraphs, we will explain the process of generating the data for this study using VMEC. For each VMEC equilibrium, we pick two different radially local regions – equilibria that satisfy (2.6) and are localized to a flux surface. It is important to point out that for most of this paper, we will only investigate modes that have small wavelengths perpendicular to the field line, i.e. modes that are localized to a flux surface, henceforth referring to our study as a local stability analysis. Since our aim is to have ample variability in our input data, at the end of this section we justify our choices by looking at the chosen flux surfaces and their corresponding $\beta$ values.

   We produce high-radial-resolution equilibria using the fixed-boundary solver in VMEC after providing it with an L-mode-like pressure profile $p = p(s)$ – a profile that does not have a sudden drop in pressure over a short radial distance, a monotonic safety factor $q = q(s)$ profile as a function of the normalized toroidal flux $s = \chi/\chi_{\mathrm{LCFS}}$ and the Last Closed Flux Surface (LCFS) shape. We choose a simple form for the profiles $p = p(s)$ and $q = q(s)$ given by

$$\left. \begin{array}{c} p = nT, \quad p_0 = \tilde{p}_0 n_0 T_0 \\ n(s) = n_0(1 + \nu_n)(1 - s^2)^{\nu_n}, \quad T(s) = T_0(1 + \nu_T)(1 - s^2)^{\nu_T} \\ q = q_0(1 + s^{2\nu_q})^{1/(2\nu_q)} \end{array} \right\}. \tag{2.8}$$

The different parameters are given in table 1. The parameter $\tilde{p}_0 \in [1, 10, 70]$ for the low, intermediate and high-beta equilibria, respectively. For each triangularity value, we choose a different LCFS shape described by a Miller parameterization (Miller *et al.* 1998)

$$\left. \begin{array}{c} R = R_0 + a\cos(t + (\sin^{-1}\delta)\sin t), \\ Z = a\kappa\sin(t). \end{array} \right\} \tag{2.9}$$

The parameter $t$ varies in the range $[-\pi, \pi)$. The values of the rest of the parameters in (2.9) are given in table 2. The radial coordinate that we will use for all the stability analyses is $\rho = \sqrt{s} = \sqrt{\chi/\chi_{\mathrm{LCFS}}}$ since it is a better measure of the radial distance from the magnetic axis than the normalized poloidal flux $\psi/\psi_{\mathrm{LCFS}}$. The safety factor and pressure profiles as a function of $\rho$ are given in figure 1. For all our studies, we use the same
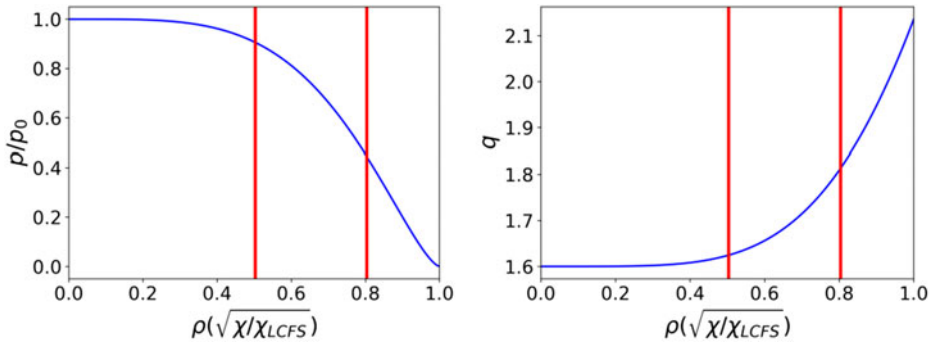
FIGURE 1. This figure shows the safety factor and normalized pressure profiles used for creating the equilibria. The two red lines correspond to the values of the normalized radius $\rho$ at which the local equilibria will be analysed for their stability.

| $n_0$ (m$^{-3}$) | $\nu_n$ | $T_0$ (eV) | $\nu_T$ | $q_0$ | $\nu_q$ | $\chi_{\text{LCFS}}$ (T m$^2$) |
|---|---|---|---|---|---|---|
| $5 \times 10^{20}$ | 0.4 | 10 | 1.1 | 1.6 | 1.2 | 1.0 |

TABLE 1. VMEC equilibria input parameters. Throughout this study, in this table, every parameter remains fixed.

| $R_0$ (m) | $a$ (m) | $\delta$ | $\kappa$ |
|---|---|---|---|
| 1.6 | 0.6 | $\pm 0.4$ | 1.3 |

TABLE 2. Miller parameters for the outer boundary.

safety factor $q$ and the normalized pressure profile $p$ with different values of $\tilde{p}_0$. In this way, we are able to create three different pressure profiles with on-axis $\beta \sim 0.01, 0.1, 1$ corresponding to $\tilde{p}_0 = 1, 10, 70$, respectively. Henceforth, we will refer to the equilibria with $\tilde{p}_0 = 1, 10, 70$ as low, intermediate and high-$\beta$ or $\beta \sim 0.01$, $\beta \sim 0.1$ and $\beta \sim 1$, respectively. We need to pick flux surfaces for our local stability analyses. In this study, we choose surfaces at normalized radii $\rho = 0.5$ and $0.8$. In total, there are twelve local equilibria in our study: $3\beta$ values $\times 2$ boundary shapes $\times 2\rho$ values. Because $\beta$ varies over a flux surface, it will be convenient to introduce a reference magnetic field for each global equilibrium and redefine

$$\beta(\rho) = 2\mu_0 p(\rho)/B_N^2, \tag{2.10}$$

$$B_N = \chi_{\text{LCFS}}/(\pi a_N^2), \tag{2.11}$$

where $B_N$ is a reference magnetic field and $a_N$ is the effective minor radius such that $\pi a_N^2$ is equal to the area enclosed by the boundary and $\chi_{\text{LCFS}}$ is the toroidal flux enclosed by the LCFS. For this study, $a_N = 0.684$ m, $B_N = 0.681$ T. The values of $\beta$ obtained from VMEC are given in table 3.

Each equilibrium has 512 surfaces with each surface represented by 40 poloidal modes. We found that the equilibria were converged with this choice of resolution. All the

| $\delta$ | $\rho$ | Low-$\beta$ | Intermediate-$\beta$ | High-$\beta$ |
|---|---|---|---|---|
| 0.4 | 0.5 | 0.011 | 0.11 | 0.77 |
| 0.4 | 0.8 | 0.006 | 0.064 | 0.45 |
| −0.4 | 0.5 | 0.011 | 0.11 | 0.77 |
| −0.4 | 0.8 | 0.006 | 0.064 | 0.45 |

TABLE 3. Reference $\beta$ values for selected surfaces.

| $\rho$ | $a_N/L_{T_i}^{\mathrm{nom}}$ | $a_N/L_{n_i}^{\mathrm{nom}}$ | $a_N/L_{p_i}^{\mathrm{nom}}$ | $a_N/L_{T_e}^{\mathrm{nom}}$ | $a_N/L_{n_e}^{\mathrm{nom}}$ | $a_N/L_{p_e}^{\mathrm{nom}}$ |
|---|---|---|---|---|---|---|
| 0.5 | 0.59 | 0.21 | 0.80 | 0.59 | 0.21 | 0.80 |
| 0.8 | 3.00 | 1.09 | 4.09 | 3.09 | 1.09 | 4.09 |

TABLE 4. Nominal gradient scale length values.
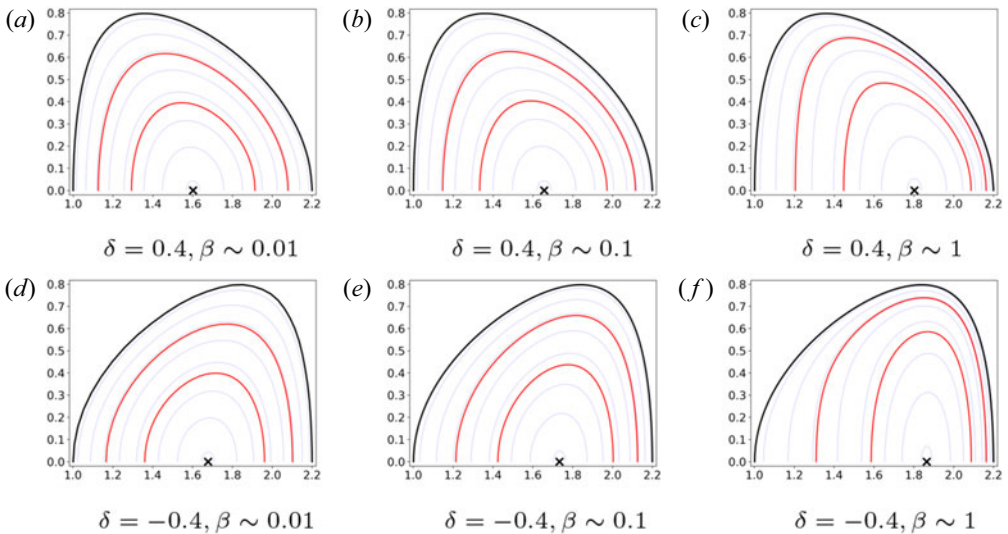


FIGURE 2. This figure shows the flux surfaces for all the equilibria generated using VMEC. The local equilibria that will be studied in this paper are highlighted in red. The magnetic axis in each figure is the black cross.

equilibria that we investigate in this study are up–down symmetric which is why we only show the upper half. The flux surface contours for the twelve equilibria are shown in figure 2.

The numerical high-$\beta$ equilibria show qualitative features like the vertical 'core' on the inboard side and thin boundary layer on the outboard side as shown by Hsu *et al.* It is interesting to see that the negative-triangularity equilibria high-$\beta$ equilibria are more strongly shaped than the positive-triangularity ones – the vertical inboard solution causes
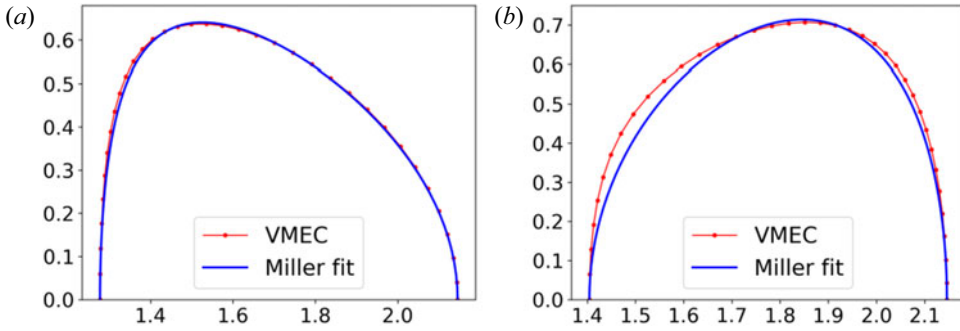
(*a*)

(*b*)

FIGURE 3. This figure shows two high-$\beta$ equilibria and their corresponding best-Miller fit. We can see that the fit for the negative triangularity is worse due to the 'squareness' of the flux surface on the inboard side. The agreement between gradients of various physical quantities will be even worse.

the flux surface to develop a 'squareness'. We illustrate the 'squareness' in figure 3.[1] Most importantly, these numerical equilibria do not suffer from any of the issues observed in Hsu et al. Therefore, all the resulting geometric coefficients are smooth which allows the local stability analyses in the following sections.

### 3. Infinite-$n$ ideal-ballooning stability

In this section, we will investigate the equilibria generated in the previous sections for their stability to ideal-ballooning modes. In §3.1, we describe the physics basis and mathematical formulation of the ideal-ballooning problem. In §3.2, we review the tools for locally varying equilibria and introduce the concept of an $\hat{s} - \alpha_{\mathrm{MHD}}$ analysis. In the final section, we present the results from our study and discuss their implications.

#### 3.1. *Physical and mathematical description*

One of the most important MHD instability for us to investigate is the ideal-ballooning instability (Connor, Hastie & Taylor 1979) – a field-aligned, pressure-driven Alfvén wave that grows when the destabilizing pressure gradient in the region of 'bad' curvature exceeds the stabilizing effect of field-line bending. The region of 'bad' curvature is a region of a flux surface where $\boldsymbol{\kappa} \cdot \nabla p > 0$, such that the field-line curvature is in the same direction as the plasma pressure gradient. For most tokamak equilibria, this region lies on the outboard side.

The equation governing the ideal-ballooning mode can be obtained by minimizing the ideal-MHD energy integral (Bernstein *et al.* 1958) for incompressible modes in the limit of large toroidal mode number. Doing so gives us a differential equation that determines $X$, the radial displacement of said mode along a field line. To ensure that the displacement $X$ satisfies the periodicity condition on the surface of interest and nearby surfaces, one uses the ballooning transformation

$$X = \sum_{N=-\infty}^{\infty} \hat{X}(\theta - 2\pi N) \, \mathrm{e}^{\mathrm{i}n(\phi - q(\theta - \theta_0 - 2\pi N)))}, \quad N \in \mathbb{Z}, \tag{3.1}$$

---

[1]Note that we use Miller fit in figure 3 to demonstrate the strong shaping of high-$\beta$ equilibria. We do not use Miller parametrization to calculate geometric coefficients in this work.

subject to the condition

$$\lim_{\theta \to \pm\infty} \hat{X}(\theta; \psi, \theta_0) = 0, \tag{3.2}$$

and solves for $\hat{X}$. The variable $n$ is the toroidal mode number, $\theta_0$ is the ballooning parameter[2] and the rest of the terms are defined in § 2. Upon minimizing the ideal-MHD energy integral and using the ballooning transformation, one obtains the ideal ballooning equation (Connor *et al.* 1979; Dewar & Glasser 1983)

$$\frac{1}{\mathcal{J}} \frac{\partial}{\partial \theta} \left( \frac{|\boldsymbol{\nabla}\alpha|^2}{\mathcal{J} B^2} \frac{\partial \hat{X}}{\partial \theta} \right) + 2 \frac{\mathrm{d}p}{\mathrm{d}\psi} \left[ \boldsymbol{B} \times \boldsymbol{\nabla} \left( \mu_0 p + \frac{B^2}{2} \right) \cdot \boldsymbol{\nabla}\alpha \right] \hat{X} = \rho \omega^2 \frac{|\boldsymbol{\nabla}\alpha|^2}{B^2} \hat{X}, \tag{3.3}$$

where $\rho$ is the plasma mass density and $\hat{X} = \hat{X}(\theta; \psi, \theta_0)$ is the eigenfunction in ballooning space and $\omega^2$ is the eigenvalue. The ballooning equation balances the stabilizing field-line bending term and destabilizing pressure gradient with the inertia of the resulting Alfvén wave, oscillating with a frequency $\omega$. Note that (3.3) depends on $\psi$ only as a parameter and we can compute the coefficients from the on-surface equilibrium quantities and their first derivatives. Therefore, it is possible to study the ballooning stability of the local equilibria that we chose in the previous section.

Due to the self-adjoint nature of ideal-MHD, all the eigenvalues ($\omega^2$) of (3.3) will be real numbers. Hence, $\omega$ will either be purely real, an oscillating mode or purely imaginary, a growing mode. We refer to the oscillating modes as stable and growing modes as unstable. Since unstable modes are of more significance to us, we will plot the normalized growth rate when plotting the results in § 3.3. We define the normalized growth rate as follows:

$$\gamma = -\mathrm{i}\omega a_N / v_{\mathrm{th},i}, \tag{3.4}$$

where $v_{\mathrm{th},i} = \sqrt{2T_i/m_i}$ is the ion-thermal velocity and $T_i$ and $m_i$ are the temperature and mass of the ions, respectively. We do this to establish a common normalization scheme throughout the paper.

### 3.2. *The Greene–Chance analysis*

To better understand the stability of a local equilibrium, we need the ability to vary that equilibrium. This can be done by changing the magnetic shear and pressure gradient independently about their nominal values – equivalent to varying the gradients of both the local current and plasma pressure – quantities that determine the solution to (2.6). This gives us the ability to generate multiple local equilibria satisfying the Grad–Shafranov equation and do a stability analysis without recalculating the global equilibrium. We define

$$\hat{s} = \frac{\rho}{q} \frac{\mathrm{d}q}{\mathrm{d}\rho}, \tag{3.5}$$

$$\alpha_{\mathrm{MHD}} = -\frac{2\mu_0 \rho q^2}{\epsilon B_N^2} \frac{\mathrm{d}p}{\mathrm{d}\rho}, \tag{3.6}$$

as the magnetic shear and pressure gradient, respectively. This method of varying a local equilibrium through $\hat{s}$ and $\alpha_{\mathrm{MHD}}$ is known as an $\hat{s} - \alpha_{\mathrm{MHD}}$ analysis. This technique was developed by Greene & Chance (1981) and has been used extensively to study local

[2]In the context of infinite-$n$ ideal-ballooning mode analyses, there is a value of the ballooning parameter $\theta_0$ at which the ballooning mode is the least stable. To find this value, one treats $\theta_0$ as a parameter and scans over its values to find the $\theta_0$ for which $\omega^2$ is the smallest.
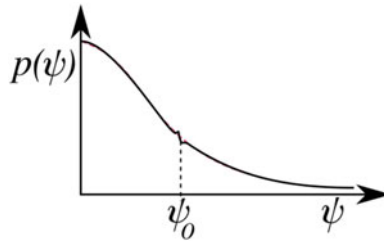
FIGURE 4. This figure summarizes the idea of Greene and Chance. The new pressure profile (black) with localized variation over the flux surface $\psi = \psi_0$ lies over the equilibrium profile (dashed red). Even though the variation in pressure at $\psi = \psi_0$ is small, the change in the pressure gradient can be large.

stability of different axisymmetric equilibria (Connor, Hastie & Taylor 1978; Connor *et al.* 1979; Bishop 1985; Miller *et al.* 1998). Figure 4 illustrates the main point – we can change the gradient of the pressure and the safety factor locally by a finite amount without significantly changing their respective values. We will use this idea again in §§ 5 and 6 to vary the pressure gradient at the nominal magnetic shear when we examine the microstability of different equilibria. Details explaining the Greene–Chance analysis are given in Appendix C.

To obtain useful maximum growth rate scans it is computationally advantageous to know where the equilibrium transitions from being stable to unstable, i.e. the region of marginal stability. This is because stable modes are extended and require many more points and a wider range in $\theta$ than unstable modes, leading to a longer computation time. To that end, we first integrate the marginally stable ballooning equation

$$\frac{1}{\mathcal{J}} \frac{\partial}{\partial \theta} \left( \frac{|\nabla \alpha|^2}{\mathcal{J} B^2} \frac{\partial \hat{X}}{\partial \theta} \right) + 2 \frac{\mathrm{d}p}{\mathrm{d}\psi} \left[ \boldsymbol{B} \times \nabla \left( \mu_0 p + \frac{B^2}{2} \right) \cdot \nabla \alpha \right] \hat{X} = 0, \qquad (3.7)$$

along the field and count the zeros of the function $\hat{X}(\theta)$ – if $\hat{X}$ has at least one zero, the mode is unstable, else it is stable. This criterion was originally developed by Newcomb (1960) for a screw pinch. He used it as a method to asses the stability of a screw pinch without explicitly finding the growth rates or the eigenfunctions. It is briefly explained in Appendix D. Using this criterion, one can obtain the sign of $\gamma^2$ and infer the stability significantly more rapidly than by exactly solving (3.3). Coupling Newcomb's criterion with the Greene–Chance analysis gives us the ability to scan the $\hat{s} - \alpha_{\mathrm{MHD}}$ space and plot the marginal stability contour ($\gamma = 0$) cheaply. For axisymmetric equilibria, the marginal stability contour is a single continuous line. Upon obtaining the contour, we choose a region around it where we solve (3.3).

To solve (3.3) we use the procedure described by Sanchez *et al.* (2000). Our two-part code[3] first finds the contour of marginal stability, then takes a region around the contour in the $\hat{s} - \alpha_{\mathrm{MHD}}$ space and implements the algorithm given in Sanchez *et al.* (2000). It outputs the maximum eigenvalue and the corresponding eigenfunction for each value of $\hat{s}$ and $\alpha_{\mathrm{MHD}}$. The plots of the maximum eigenvalue along with the curve of marginal stability are shown in the next section.[4]

---

[3]Our Python code is freely available at https://github.com/rahulgaur104/ideal-ballooning-solver.

[4]All the calculations in this work are done for $\theta_0 = 0$. A more complete picture would require one to scan over multiple values of $\theta_0$ and take the union of the resulting marginal stability curves and growth rate plots. Finite $\theta_0$ effects may modify the second-stability boundary.
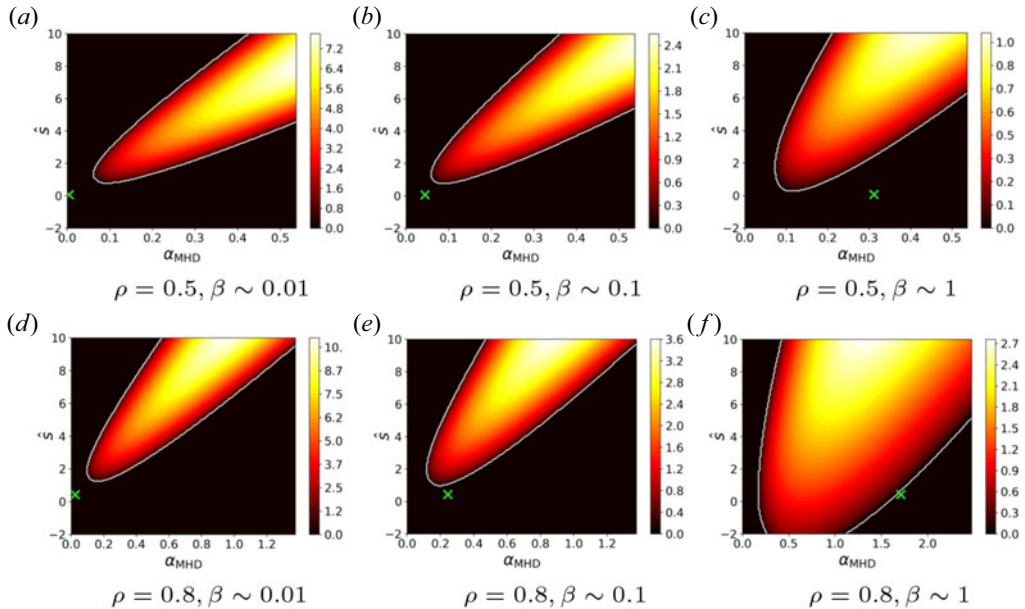
FIGURE 5. This figure shows the normalized growth rate $\gamma a_N / v_{\mathrm{th},i}$ contours along with the curve of marginal stability (white line) for the positive-triangularity equilibria. Columns correspond to the low, intermediate and high-$\beta$ regimes, respectively. The nominal equilibrium value is given by the green cross. The difference between the growth rates from the low and high-$\beta$ equilibria is due to our choice of normalization in (3.4).

### 3.3. *Ideal-ballooning analysis results*

This section contains the results of the $\hat{s} - \alpha_{\mathrm{MHD}}$ analyses of the twelve local equilibria that we chose in § 2.1. We plot a 2-D contour plot of the magnitude of the growth rate as defined by (3.4). We begin by discussing the positive-triangularity equilibria in figure 5.

All the positive-triangularity equilibria studied here are stable at their nominal values. The low-$\beta$ equilibria lie below the marginal stability contour whereas the high-$\beta$ equilibria lie above it. For low-$\beta$ equilibria the ballooning threshold is well known to be $\alpha_{\mathrm{MHD}} \sim 1$ but for the high-$\beta$ equilibria, using (3.6), $\alpha_{\mathrm{MHD}} \sim 1/\delta_{\mathrm{Hsu}}^2 \gg 1$ which pushes these equilibria into the region of 'second' stability, first discovered by Greene & Chance (1981). Note that the high-$\beta$ equilibrium in figure 5($f$) is close to marginally stable. Also, since ballooning modes are Alfvén waves and we use ion-thermal speed in (3.4), we see that the maximum growth rate decreases as $v_{\mathrm{th},i}/v_A = \sqrt{\beta/2}$ –high-$\beta$ equilibria having the smallest maximum growth rates. This non-conventional choice of normalization will help us quantitatively compare ideal-ballooning growth rates with the ones obtained from various microstability studies in §§ 5–7. In the next paragraph, we discuss the results from the ideal-ballooning scans of the negative-triangularity equilibria.

In figure 6, we can see the nominal equilibria for the negative triangularity are stable for all cases except figure 6($e$). The trends follow those of the positive-triangularity equilibria with one important exception. Unlike the positive-triangularity equilibria, the high-$\beta$ negative-triangularity equilibria move closer to the marginal stability boundary in the inner core region as seen in figure 6($c$). This is different from the usual result – ballooning-stable equilibria with peaked pressure profiles approach marginal stability as we move towards the boundary and pressure gradient gets steeper (as seen in figures 5, 6$a$,
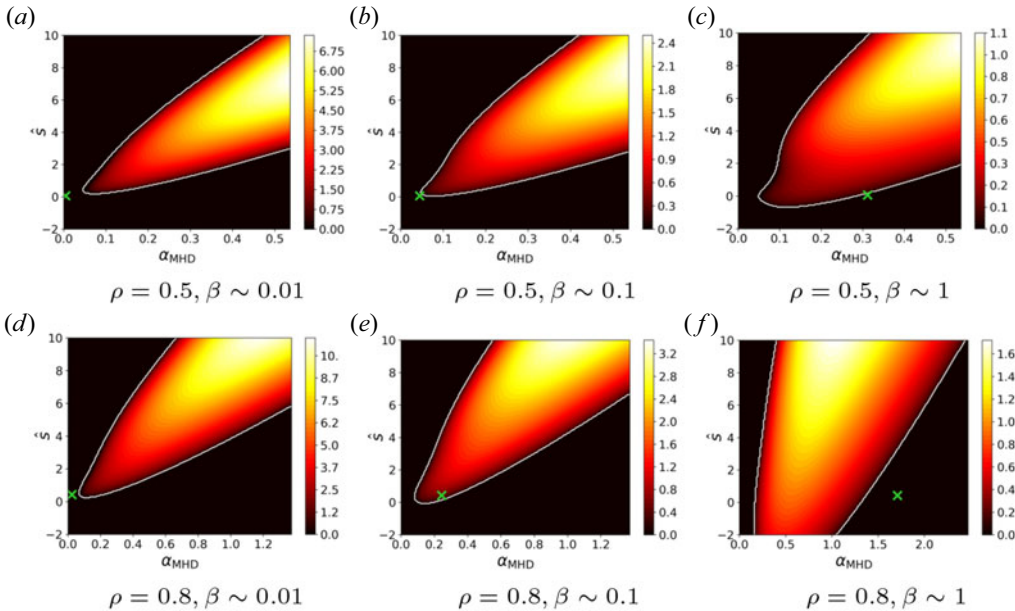
FIGURE 6. This figure shows the normalized growth rate contours along with the curve of marginal stability for the negative-triangularity equilibria. The nominal equilibrium value is denoted by the green cross; (*a*) $\rho = 0.5, \beta \sim 0.01$, (*b*) $\rho = 0.5, \beta \sim 0.1$, (*c*) $\rho = 0.5, \beta \sim 1$, (*d*) $\rho = 0.8, \beta \sim 0.01$, (*e*) $\rho = 0.8, \beta \sim 0.1$ and (*f*) $\rho = 0.8, \beta \sim 1$.

6*b*, 6*d* and 6*e*) – indicating that negative-triangularity, high-$\beta$ equilibria have enhanced ballooning stability in the outer core. We will observe a similar trend when we present results from the electromagnetic microstability analyses in § 7.

Recently, Davies, Dickinson & Wilson (2022) have published a study investigating access to high-$\beta$ spherical tokamak equilibria where they find that high-$\beta$, negative-triangularity equilibria are more unstable and less accessible than their positive-triangularity counterparts. At first, this may seem to contradict our results. However, looking at the plasma $\beta$ values in Davies *et al.*, we realize that their high-$\beta$ equilibria correspond to intermediate-$\beta$ in our work. Indeed, the negative-triangularity intermediate-$\beta$ equilibrium in figure 6(*e*) is ballooning unstable whereas the positive-triangularity equilibrium in figure 5(*e*) is ballooning stable. Furthermore, Davies *et al.* define accessibility as the ability to reach the nominal $\alpha_{MHD}$ from $\alpha_{MHD} = 0$ at the nominal $\hat{s}$ – a straight line in $\hat{s} - \alpha_{MHD}$ space – the actual path of an equilibrium from startup to a steady-state operation in the $\hat{s} - \alpha_{MHD}$ space is a 2-D curve, similar to figures 2(*a*) and 2(*b*) in Chance *et al.* (1990). Therefore, our results corroborate rather than contradict the findings in Davies *et al.*

The most important takeaway from this study is that all low- and high-$\beta$ equilibria are stable to ideal-ballooning mode. This indicates that it might be possible to generate high-$\beta$ equilibria that are ballooning stable.[5] Even though one of the intermediate-$\beta$ equilibria is unstable, we will use it in our study as it will help us understand the behaviour of microstability with changing $\beta$.

<hr>

[5]Note that we do not prove the experimental accessibility of these high-$\beta$ equilibria. We show that if these equilibria were to exist, they will be stable to the ideal-ballooning mode. The problem of accessibility in the context of ideal-ballooning stability was studied by Chance *et al.* (1990).

## 4. Microstability analysis

This section contains the general theoretical and numerical details of our microstability analysis. In §4.1, we will explain the physical basis and theoretical details of the gyrokinetic model. In the next section, we will explain how the model is implemented numerically using the GS2 code and provide the general details of our numerical study.

### 4.1. *The gyrokinetic model*

The electromagnetic gyrokinetic model is a simplification of the $6D$ Vlasov–Maxwell system of equations to a $5D$ system that predicts the self-consistent evolution of a distribution of charged particles and its electromagnetic fields in the presence of low-frequency, small-scale fluctuations. We define the distribution and fields as

$$\left.\begin{aligned} f_s &= F_{0s} + \delta f_s, \\ \boldsymbol{E} &= \boldsymbol{E}_0 + \delta \boldsymbol{E}, \\ \boldsymbol{B} &= \boldsymbol{B}_0 + \delta \boldsymbol{B}, \end{aligned}\right\} \tag{4.1}$$

where the fields comprise their equilibrium components (with a subscript 0) plus small fluctuations. The fluctuations $\delta f_s$, $\delta \boldsymbol{E}$ and $\delta \boldsymbol{B}$ are defined such that they vanish when averaged over length and time scales much larger than the particle gyroradius $\rho_s$ and turbulence frequency $\omega$, respectively. The gyrokinetic model is derived in the limit

$$\tilde{\epsilon} \equiv \frac{\omega}{\Omega_s} \sim \frac{\rho_s}{a_N} \sim \frac{k_\parallel}{k_\perp} \sim \frac{\delta f_s}{F_{0s}} \sim \frac{Z_s e \varphi}{T_s} \sim \frac{|\delta \boldsymbol{B}|}{|\boldsymbol{B}_0|} \ll 1, \tag{4.2}$$

where $\Omega_s = (Z_s e B)/(m_s c)$ is the cyclotron frequency and subscript $s$ denotes the species. The variable $\varphi$ is the perturbed electrostatic potential. The particle gyroradius $\rho_s$, given by

$$\rho_s \equiv \frac{v_{\text{th},s}}{\Omega_s}, \tag{4.3}$$

is the perpendicular length scale of the turbulent fluctuations and $v_{\text{th},s} = \sqrt{(2T_s)/m_s}$ is the thermal velocity. The length scale $a_N$ is the effective minor radius, defined in §2.1. The wavenumbers of the mode perpendicular and parallel to the equilibrium magnetic field are denoted by $k_\perp$ and $k_\parallel$, respectively.

In the small $\tilde{\epsilon}$ limit, one can reduce the dimensionality of the problem from $6D(\boldsymbol{r}, w_\perp, w_\parallel, \vartheta)$ to $5D(\boldsymbol{r}, w_\perp, w_\parallel)$ by averaging over the gyrophase $\vartheta$. For this $5D$ coordinate system, we will transform back and forth between two different coordinates, the particle position and velocity coordinates $(\boldsymbol{r}, w_\perp, w_\parallel, t)$ and the guiding-centre coordinates $(\boldsymbol{R}_s, E_s, \mu_s, t)$ where

$$E_s = \frac{1}{2} m_s w^2, \tag{4.4}$$

$$\mu_s = \frac{m_s w_\perp^2}{2B}, \tag{4.5}$$

are the total kinetic energy and the magnetic moment of the particle. The guiding centre is given in terms of the particle position by the Catto transformation (Catto & Tsang 1977)

$$\boldsymbol{R}_s = \boldsymbol{r} - \frac{\boldsymbol{b} \times \boldsymbol{w}_\perp}{\Omega_s}. \tag{4.6}$$

The gyroaveraging operators $\langle\rangle_{R_s}$ and $\langle\rangle_r$

$$\langle X \rangle_{R_s} = \frac{1}{2\pi} \int_0^{2\pi} X(r) \, \mathrm{d}\vartheta, \tag{4.7}$$

$$\langle X \rangle_r = \frac{1}{2\pi} \int_0^{2\pi} X(R_s) \, \mathrm{d}\vartheta, \tag{4.8}$$

denote the average of $X$ over a gyration period at fixed guiding centre $R_s$ and at fixed position $r$, respectively. It is convenient to define the gyrokinetic model in terms of the parallel component $\delta A_\parallel$ of the magnetic vector potential, the magnetic field strength fluctuation $\delta B_\parallel$

$$\delta B_\parallel = b \cdot (\nabla \times \delta A_\perp), \tag{4.9}$$

the electrostatic potential

$$\delta E = -\nabla \varphi - \frac{1}{c} \frac{\partial A}{\partial t}, \tag{4.10}$$

and the gyrokinetic distribution function in the guiding-centre coordinate system $(R_s, E_s, \mu_s, t)$

$$h_s(R_s, E_s, \mu_s, t) = \frac{Z_s e \varphi(r, t) F_{0s}}{T_s} + \delta f_s(R_s, E_s, \mu_s, t). \tag{4.11}$$

Using these new fields we can now introduce the $\delta f$ gyrokinetic theory that was first derived for the linear electromagnetic case by Antonsen & Lane (1980) and nonlinear case by Frieman & Chen (1982). For a collisionless, linear electromagnetic model, following the notation of Abel *et al.* (2013), the governing equations are

$$\frac{\partial h_s}{\partial t} + (w_\parallel b + v_{Ds}) \cdot \frac{\partial h_s}{\partial R_s} = \frac{Z_s e F_{0s}}{T_s} \frac{\partial \langle \varphi - w \cdot \delta A/c \rangle_{R_s}}{\partial t} - V_E \cdot \nabla F_{0s}, \tag{4.12}$$

$$\sum_s \frac{(Z_s e)^2 \varphi}{T_s} = \sum_s Z_s e \int d^3 w \, \langle h_s \rangle_r, \quad \tau = \frac{T_e}{T_i}, \tag{4.13}$$

$$-\nabla_\perp^2 \delta A_\parallel = \frac{4\pi}{c} \sum_s Z_s e \int d^3 w \, w_\parallel \langle h_s \rangle_r, \tag{4.14}$$

$$\nabla_\perp^2 \frac{\delta B_\parallel B}{4\pi} = -\nabla_\perp \nabla_\perp : \sum_s \int d^3 w \, \langle m_s w_\perp w_\perp h_s \rangle_r, \tag{4.15}$$

where the velocity integrals in (4.13) are taken at fixed $r$. The velocities $V_E$ and $v_{Ds}$ are the $E \times B$ and the magnetic drift velocities, respectively,

$$V_E = \frac{c}{B} b \times \langle \nabla \varphi \rangle_R - \frac{1}{B} b \times \langle \nabla (w \cdot \delta A) \rangle_{R_s}, \tag{4.16}$$

$$v_{Ds} = \frac{w_\parallel^2}{\Omega_s} b \times (b \cdot \nabla b) + \frac{w_\perp^2}{2\Omega_s} \frac{b \times \nabla B}{B}. \tag{4.17}$$

This completely defines the linear gyrokinetic system. The gyrokinetic model is a good approximation for the core region of a tokamak plasma where our study is being conducted (White *et al.* 2013; Creely *et al.* 2017). We solve the gyrokinetic model in a 3-D flux tube – a tube with a rhombus-shaped cross-section following the field line. The appropriate

length of the flux tube and the boundary conditions at the ends are determined using the ideas developed by Beer, Cowley & Hammett (1995). All the variables are assumed to be periodic perpendicular to the field line. This allows us to further simplify (4.12) by writing the fluctuating fields as a Fourier series

$$
\left.
\begin{aligned}
h_s &= \sum_k h_{k_\perp,s}(\theta, E, \mu, t) \exp(i\boldsymbol{k}_\perp \cdot \boldsymbol{R}_s), \\
\varphi &= \sum_k \varphi_{k_\perp}(\theta, t) \exp(i\boldsymbol{k}_\perp \cdot \boldsymbol{r}), \\
\delta A_\parallel &= \sum_k \delta A_{\parallel,k_\perp}(\theta, t) \exp(i\boldsymbol{k}_\perp \cdot \boldsymbol{r}), \\
\delta B_\parallel &= \sum_k \delta B_{\parallel,k_\perp}(\theta, t) \exp(i\boldsymbol{k}_\perp \cdot \boldsymbol{r}).
\end{aligned}
\right\}
\tag{4.18}
$$

Applying this ansatz to (4.12), we obtain

$$
\left( \frac{\partial}{\partial t} - i\omega_{Ds} \right) h_{k_\perp,s} + (\boldsymbol{b} \cdot \boldsymbol{\nabla}\theta) w_\parallel \frac{\partial h_{k_\perp,s}}{\partial \theta} = \left\{ \frac{\partial}{\partial t} - i\omega_{*,s} \left[ 1 + \eta_s \left( \frac{E_s}{T_s} - \frac{3}{2} \right) \right] \right\}
$$
$$
\times \left[ J_0 \left( \frac{k_\perp w_\perp}{\Omega_s} \right) \left( \varphi_{k_\perp} - \frac{w_\parallel \delta A_\parallel}{c} \right) + J_1 \left( \frac{k_\perp w_\perp}{\Omega_s} \right) \frac{w_\perp}{k_\perp} \frac{\delta B_\parallel}{c} \right] F_{0s},
\tag{4.19}
$$

where

$$
\omega_{Ds} = \boldsymbol{k}_\perp \cdot \boldsymbol{v}_{Ds},
\tag{4.20}
$$

is the magnetic drift frequency, $J_0(k_\perp \rho_s)$ and $J_1(k_\perp \rho_s)$ are the zeroth- and first-order cylindrical Bessel functions, respectively,

$$
\frac{a_N}{L_{Ts}} = -\frac{\mathrm{d} \log(T_s)}{\mathrm{d}\rho}, \quad \frac{a_N}{L_{n_s}} = -\frac{\mathrm{d} \log(n_s)}{\mathrm{d}\rho}, \quad \eta_s = \frac{L_{n_s}}{L_{T_s}},
\tag{4.21}
$$

and

$$
\omega_{*,s} = \frac{T_s}{Z_s eB} [(\boldsymbol{b} \times \boldsymbol{k}_\perp) \cdot \boldsymbol{\nabla} \log n_s].
\tag{4.22}
$$

For this study, we choose a hydrogen plasma, i.e. $Z_i = 1, Z_e = -1$. The variables $L_{ns}$ and $L_{Ts}$ are the density and temperature-gradient scale lengths. The quantity $\omega_{*,s}$, the diamagnetic drift frequency, is the typical frequency of a drift wave – waves caused due to gradients in temperature or density. For these modes

$$
\frac{\partial}{\partial t} \sim \omega \sim \omega_{*,s}.
\tag{4.23}
$$

In §§ 5 and 6, we will investigate two types of electrostatic drift wave instabilities, the ion-temperature-gradient (ITG) mode and the trapped electron mode (TEM). For purely electrostatic modes, we solve (4.12)–(4.13) only and assume the magnetic fluctuations, $\delta A_\parallel$ and $\delta B_\parallel$ to be absent. In § 7, we investigate the effect of magnetic fluctuations by solving the full set of (4.12)–(4.15). The procedure for numerically solving the gyrokinetic model is explained in the following section.
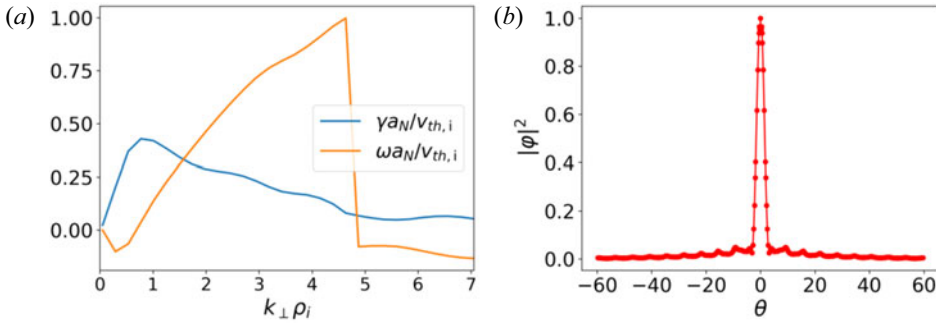
FIGURE 7. This figure shows (*a*) the output from a typical electrostatic GS2 run showing the normalized frequency and growth rate spectrum with both electron-gradient- ($\omega a_N/v_{\text{th},i} < 0$) and ion-gradient-driven ($\omega a_N/v_{\text{th},i} > 0$) instabilities and (*b*) showing the variation along the field line of the square of the normalized electrostatic potential $|\varphi|^2$. We can see that the potential is well resolved and decays sufficiently before reaching the boundaries.

### 4.2. *Using the* GS2 *code*

GS2[6] (Kotschenreuther, Rewoldt & Tang 1995*b*; Dorland *et al.* 2000; Jenko & Dorland 2001; Highcock 2012) is a parallel code that solves the gyrokinetic model as an initial-value problem. It solves (4.12)–(4.15) numerically by calculating the evolution of an initial perturbation inside a flux tube.

Before each run, one has to specify the value of the gradient scale lengths $a_N/L_{n_s}, a_N/L_{T_s}$, the range of normalized wavenumbers $k_\perp \rho_i$ and various geometric coefficients as a function of $\theta$. The values of these inputs are specific to the linear mode under consideration and will be provided in the following sections. Since we are only studying stability against fluctuations that vary on a small perpendicular scale $k_\perp \rho_i \sim 1$, we can get the geometric coefficients from the local equilibria just like we did for the ideal-ballooning stability analysis.[7]

The perpendicular structure of different fluctuations is defined by defining the wavevector $\boldsymbol{k}_\perp$ that can be written as

$$\boldsymbol{k}_\perp = k_y \nabla y + k_x \nabla x, \tag{4.24}$$

where $x$ and $y$ are normalized forms of the coordinates $\psi$ and $\alpha$, respectively. For our study, we assume $k_x = 0$, i.e. modes with no variation in the radial direction at $\theta = 0$.[8] We choose around $15-25$ values of $k_y \rho_i$ in the range $k_y \rho_i = 0.05-6$. All of our simulations are well resolved in $\theta$ and well converged as can be seen in figure 7. For this study, $\theta \in [-19\pi, 19\pi]$ and more than 450 points along the $\theta$ grid unless stated otherwise.

For the velocity space structure GS2 uses an $(E, \lambda)$ grid instead of the $(w_\parallel, w_\perp)$ grid. Defining the pitch angle as

$$\lambda(\theta_b) = \frac{\mu}{E}, \tag{4.25}$$

---

[6]The GS2 version used for this study is freely available at https://zenodo.org/record/4461680.
[7]Our VMEC to GS2 interface for calculating the geometric coefficients is freely available at https://github.com/rahulgaur104/VMEC2GK.
[8]This is equivalent to choosing $\theta_0 = 0$ in the ideal-ballooning study. The parameter $\theta_0 \sim k_x/k_y$ denotes the tilt of a turbulent eddy with respect to the $\nabla\psi$ direction. In axisymmetric, up–down symmetric equilibria, the most unstable modes almost always lie at $\theta_0 = 0$.

where $\theta_b$ is the bounce angle – the value of $\theta$ at which a trapped particle with a pitch angle $\lambda$ reflects back from a region of high magnetic field. For a given pitch angle $\lambda$, the bounce angle is defined such that $B(\theta_b) = 1/\lambda$. In GS2, resolution of the passing particle distribution function in the coordinate $\lambda$ is set by the variable nlambda. We set nlambda = 12. For the trapped particle distribution, we choose 11 bounce points. Similarly, for the energy-space resolution, we set the value of the GS2 variable negrid = 10.[9] We choose 27 points along the flux tube for every $2\pi$ interval to ensure sufficient resolution along the field line. This completely defines the resolution in GS2.

In figure 7, we show the results from a typical GS2 run. After each run, one obtains the normalized growth rate $\gamma a_N/v_{\text{th},i}$, the wave frequency $\omega a_N/v_{\text{th},i}$, the electrostatic potential eigenfunction $\varphi(\theta, t)$ for electrostatic runs and $\varphi(\theta, t), \delta A_\parallel(\theta, t)$ and $\delta B_\parallel(\theta, t)$ for electromagnetic runs. We also obtain the quasilinear particle and heat fluxes for each mode

$$\Gamma_{s,k_y} = \int \frac{\mathrm{d}\theta}{\boldsymbol{B} \cdot \boldsymbol{\nabla}\theta} \int \mathrm{d}^3 w (\boldsymbol{V}_{E,k_y} \cdot \boldsymbol{\nabla}\psi) h_{s,k_y}, \tag{4.26}$$

$$Q_{s,k_y} = \int \frac{\mathrm{d}\theta}{\boldsymbol{B} \cdot \boldsymbol{\nabla}\theta} \int \mathrm{d}^3 w (\boldsymbol{V}_{E,k_y} \cdot \boldsymbol{\nabla}\psi) E_s h_{s,k_y}, \tag{4.27}$$

where the subscript $k_y$ denotes the mode $k_y$ in the Fourier space. These quantities can be used to extract information about an unstable mode (Kotschenreuther *et al.* 2019). Since this is a linear study, the absolute values of the fluxes do not contain any useful information but their ratio $\Gamma_{s,k_y}/Q_{s,k_y}$ can still be used to characterize the type of instability. We will use this ratio for the TEM study in § 6.

## 5. The ITG study

This section contains the results and analysis of the ITG study of the equilibria that we obtained in § 2. In § 5.1, we will present the specific details, including the values of different parameters used for the simulation and the reasoning behind our choices. In § 5.2, we will introduce the local magnetic shear, a quantity that characterizes the stability of an equilibrium to the ITG mode. In the final section, we will plot and compare the results of all the different local equilibria and explain the stability of the high-$\beta$ equilibria.

### 5.1. *Details of the study*

The most important form of electrostatic instability that arises at low wavenumbers, the ITG (Cowley, Kulsrud & Sudan 1991), occurs when a drift wave becomes unstable due to a large ion temperature gradient, i.e. large $a_N/L_{T_i}$. Therefore, our objective is to understand this mode by doing a scan in the temperature-gradient scale length, $a_N/L_{T_i}$. Using the definition of the pressure $p_s = n_s T_s$, we can write

$$\frac{a_N}{L_{p_s}} \equiv -\frac{\mathrm{d}\log(p)}{\mathrm{d}\rho} = -\frac{\mathrm{d}\log(T_s)}{\mathrm{d}\rho} - \frac{\mathrm{d}\log(n_s)}{\mathrm{d}\rho} = a_N \left( \frac{1}{L_{n_s}} + \frac{1}{L_{T_s}} \right). \tag{5.1}$$

Using the equation above along with (3.6), we can write

$$\alpha_{\text{MHD}} = \frac{\beta}{2} \sum_s \frac{a_N}{L_{p_s}} \frac{\rho q^2}{2\mu_0 \epsilon}. \tag{5.2}$$

---

[9]For the sake of brevity, we have avoided explaining the details of the velocity grid. These details and resolution requirements can be found in Highcock (2012).

| $a_N/L_{n_i}$ | | | $a_N/L_{T_i}$ | | |
|---|---|---|---|---|---|
| 0.21 | 0.19 | 0.59 | 1.39 | 2.98 | 6.19 |
| 0.10 | 0.29 | 0.69 | 1.49 | 3.08 | 6.29 |

TABLE 5. Values of $a/L_{T_i}$ at $\rho = 0.5$ for the ITG study.

| $a_N/L_{n_i}$ | | | $a_N/L_{T_i}$ | | |
|---|---|---|---|---|---|
| 1.09 | | 0.95 | 3.00 | 7.10 | 15.27 |
| 0.54 | | 1.50 | 3.55 | 7.64 | 15.82 |

TABLE 6. Values of $a/L_{T_i}$ at $\rho = 0.8$ for the ITG study.

Furthermore, recall that we can vary the normalized pressure gradient $\alpha_{\mathrm{MHD}}$ for a local equilibrium using the idea of Greene and Chance without recalculating the global equilibrium. This gives us the ability to self-consistently vary the temperature and density gradient scale lengths for a fixed $\beta$ as long as we recalculate the local equilibrium for the resulting value of $\alpha_{\mathrm{MHD}}$.[10] Table 3 contains the nominal density, temperature and pressure gradient scale lengths, denoted $a_N/L_{n_i}^{\mathrm{nom}}$, $a_N/L_{T_i}^{\mathrm{nom}}$ and $a_N/L_{p_i}^{\mathrm{nom}}$, respectively.

These are the values obtained from the original local equilibrium generated by VMEC and are exactly the same for all the different beta and triangularity values. For the ITG mode study, we define

$$\mathrm{fac} = \frac{\mathrm{d}P}{\mathrm{d}\rho} \bigg/ \left( \frac{\mathrm{d}P}{\mathrm{d}\rho} \right)_{\mathrm{nom}}, \tag{5.3}$$

as the ratio of actual pressure to the nominal pressure. We choose $\mathrm{fac} = (0.5, 1, 2, 4, 8)$ times the nominal pressure gradient for $\rho = 0.5$ and $\mathrm{fac} = (0.5, 1, 2, 4)$ times the nominal pressure gradient for $\rho = 0.8$. For each pressure gradient, we choose two density gradient scale lengths – the nominal and half of the nominal value from the local VMEC equilibrium while varying the temperature gradient scale length consistently for each gradient scale length. Tables 5 and 6 contain the resulting values.

These 18 values of various scale lengths are exactly the same for all the triangularities as well as for all the different beta values due to the way we have defined $\rho$. From previous observations and studies, we know that the typical peak ITG growth rate lies around $k_y\rho_i = 1$. To capture the maximum growth rate, we calculate the growth rates in the range $k_y\rho_i \in [0.05, 2]$. For ITG, we have made the common assumption of adiabatic electrons to exclude the effect of kinetic electrons on the ITG mode and avoid other modes like the TEM. Mathematically, this means one assumes $h_{e,k_y} = 0$ when solving (4.19) for the electrons.

Using the values in tables 5 and 6, we run GS2 in the electrostatic limit ($\delta A_\parallel = 0$, $\delta B_\parallel = 0$) and obtain the maximum normalized growth rate $\gamma a_N/v_{\mathrm{th},i}$ for each of the 108 cases, 18 for each beta and each triangularity value. The results showing comparison between different beta values, boundary shapes and normalized radii will be shown in § 5.3. We expect the equilibria to become more stable to the ITG mode as we increase $\beta$. This behaviour is well-known (Jarmén, Malinov & Nordman 1998; Hirose 2000) in the

[10]Maintaining self-consistency is crucial to all local analyses. Violating (5.1) can give rise to specious, non-physical instabilities (Zhu *et al.* 2020).

literature for low and intermediate-$\beta$ equilibria. To try and explain this trend, in the next section we look as the local shear as a characteristic quantity that explains stabilization of the ITG mode with increasing $\beta$.

### 5.2. *Characterizing stability to the ITG mode*

In this section, we define and plot an important quantity, the local magnetic shear (Greene & Chance 1981), which will help us understand the response of a local equilibrium to the ITG mode. We use the local shear since negative global shear $\hat{s}$ is known to stabilize ITG (Uchida *et al.* 2003). In the following section, we will plot the local shear as a function of $\theta_{\mathrm{geo}}$ at the nominal $\hat{s}$ and $\alpha_{\mathrm{MHD}}$ for the high-$\beta$ equilibria and compare it with the low, intermediate and a low-$\beta$ shifted-circle equilibrium (abbreviated as SC in the plots). We will show that the behaviour of ITG is directly related to the local shear and argue that a large negative local shear over a wide range along the field lines stabilizes the ITG mode. Mathematically, the local shear $\nu$ is given by (Greene & Chance 1981; Dewar & Glasser 1983)

$$\nu = -\boldsymbol{B} \cdot \boldsymbol{\nabla}_N \left( \frac{\boldsymbol{\nabla}_N \alpha \cdot \boldsymbol{\nabla}_N \psi}{|\boldsymbol{\nabla}_N \psi|^2} \right), \tag{5.4}$$

where $\boldsymbol{\nabla}_N = a_N \boldsymbol{\nabla}$ is used to non-dimensionalize $\nu$. We will plot the local shear as a function of the geometric poloidal angle defined in the figure 8. The coordinate $\theta_{\mathrm{geo}}$ is advantageous as it, unlike $\theta$, is a physically intuitive poloidal angle. Mathematically, $\theta_{\mathrm{geo}}$ is a monotonic function of $\theta - \nu$ can always be transformed to $\hat{\kappa}(\theta)$ and *vice versa*. To plot $\nu$ with respect to $\theta_{\mathrm{geo}}$, we further simplify (5.4)

$$\nu = -\frac{F}{qR^2} \left[ \left( \frac{qF'}{F} + F'F \frac{q}{(R_s B_{ps})^2} \right) + \frac{qp'}{B_{ps}^2} + \frac{2q}{R_s B_{ps}} \left( \frac{\sin(u)}{R_s} - \frac{1}{R_c} \right) \right]. \tag{5.5}$$

The symbols used and formalism needed to derive (5.5) is given in Appendix C. It is important to point out that

$$\hat{s} = \frac{\rho |\boldsymbol{\nabla}_N \psi|}{2\pi q a_N^2} \int_0^{2\pi} \frac{\mathrm{d}\theta \, \mathrm{d}\phi}{\boldsymbol{B} \cdot \boldsymbol{\nabla}_N \theta} \nu. \tag{5.6}$$

Thus, the appropriately weighted average of the local shear over a flux surface gives us the global magnetic shear $\hat{s}$. The global shear is held fixed for all the local equilibria at a given $\rho$. This relation implies that the local shear can be negative for a given range in $\theta$ for a positive global shear $\hat{s}$. Finally, we plot local shear at nominal $\hat{s}$ and $\alpha_{\mathrm{MHD}}$ in figure 9 for different beta values.

The local shear depends on the pressure gradient $\alpha_{\mathrm{MHD}}$ which further depends on $\beta$ as well as the gradient scale lengths $L_n$ and $L_T$. The beta value increases the local negative shear through the Shafranov shift. The gradient scale length does so by increasing the poloidal current gradient $\mathrm{d}F/\mathrm{d}\rho$ required to balance the pressure gradient which consequently increases the toroidal magnetic field. A plot showing the effect of pressure gradient on the local shear is shown in figure 13(*a*). Note that in our scans decreasing the pressure gradient scale length increases the driving term $\eta = L_n/L_T$. In fact, in this study, for a given $\beta$, $\eta$ increases faster than $a_N/L_p$. A plot of $\eta$ versus the pressure gradient scaling factor is shown in figure 10.

The dominant mechanism for generating negative local shear is the $\beta$-induced Shafranov shift. The local shear may also depend on the shaping, especially for negative triangularities. However, we find that shaping does not have a significant effect on the ITG stability of the high-$\beta$ equilibria.
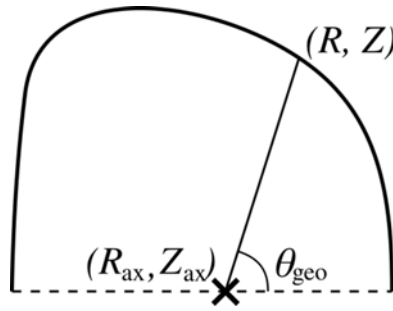
FIGURE 8. This figure illustrates the definition of $\theta_{\text{geo}}$. The coordinates of the magnetic axis, marked with a cross, are $(R_{\text{ax}}, Z_{\text{ax}})$.
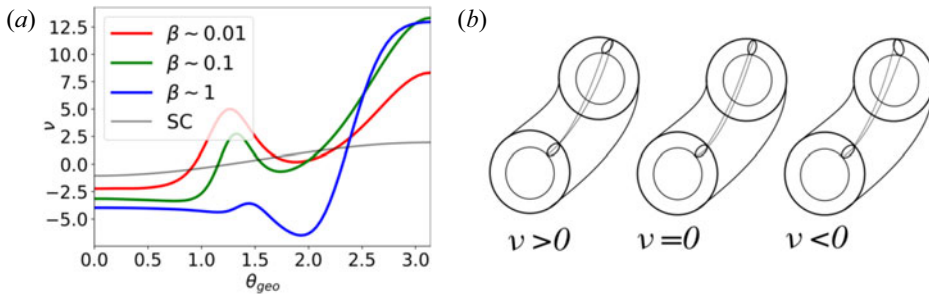


FIGURE 9. This figure explains the physical meaning of the local magnetic shear with (*a*) showing a typical local shear plot of negative triangularity equilibria at the nominal $\hat{s} = 0.45$ and nominal $\alpha_{\text{MHD}}$ values at $\rho = 0.8$ for different beta values and a low-$\beta$ shifted-circle model (abbreviated SC). (*b*) Illustrates a modified interpretation from Antonsen *et al.* (1996) explaining the concept of local magnetic shear. Negative local shear twists the turbulent eddies more than positive or zero local shear in the region of bad curvature, stabilizing the ITG mode.
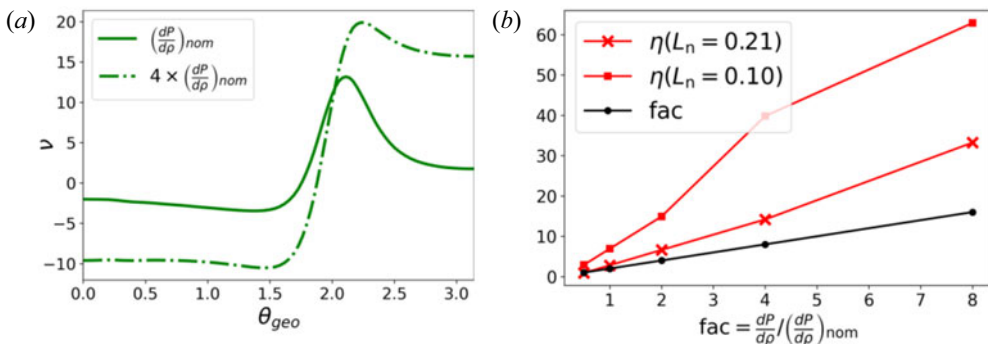


FIGURE 10. This shows (*a*) the change in the local shear for fac $= 4$ (increased pressure gradient). The local shear is much more negative with an approximately linear dependence with fac on outboard side. On the other hand, (*b*) shows the comparison between the ITG driving term $\eta$ and the pressure gradient scaling factor fac. The term $\eta$ is calculated using the values given in table 5. We can see that $\eta$ grows linearly, but with a larger pre-factor. These figures illustrate how the ITG driving term grows more rapidly than the stabilizing local shear as we increase the pressure gradient.
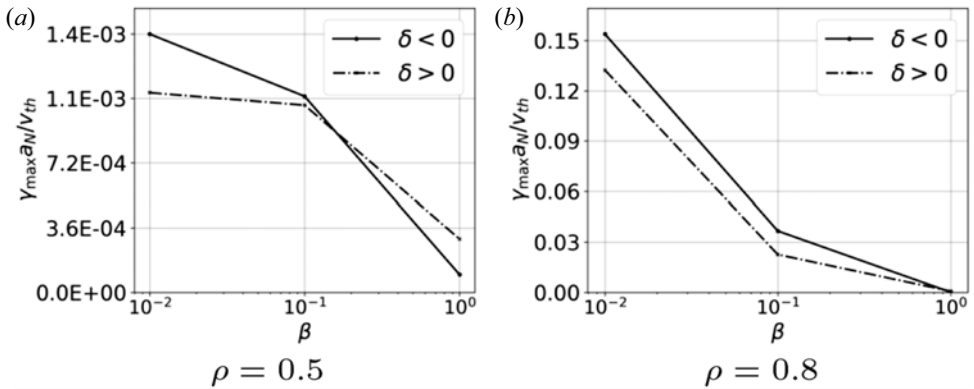
FIGURE 11. These plots show the ITG $\max(\gamma a_N/v_{\text{th},i})$ (over $k_y\rho_i \in [0.05, 2]$) vs the typical $\beta$ for nominal equilibria at different radial locations.

### 5.3. *The ITG results*

Since GS2 is an initial-value code, resolving a growth rate $\gamma \leq \gamma_{\text{thresh}}$ would require us to run the simulation for at least $t \sim 1/\gamma_{\text{thresh}}$. For large wavenumbers and a semi-implicit time-stepping scheme, it leads to a relatively high runtime cost. Hence, we define a small positive 'threshold' growth rate $\gamma_{\text{thresh}}$ which we will use to separate stable and unstable modes. If the maximum ITG growth $\max(\gamma a_N/v_{\text{th},i}) < \gamma_{\text{thresh}}$, we classify it as stable. For this study, we choose $\gamma_{\text{thresh}} = 0.005$.

We find that all the nominal equilibria stabilize as we increase $\beta$ as first noted by Candy & Waltz (2003*a*) – the high-$\beta$ equilibria are stable to the ITG mode, as shown in figure 11 below. To better understand what causes this effect, we do a scan in gradient scale length scales given in tables 5 and 6. Each group of plots contains maximum growth rate for a range of $a/L_{T_i}$ at a fixed $a/L_{n_i}$ for the three beta values. Plots are grouped by the triangularity of the equilibria. For each group, there are subgroups based on the normalized radius $\rho$. The results corresponding to the positive-triangularity boundary shape are shown in figure 12.

In figure 11, one observes that, for the high-$\beta$ cases, the ITG mode is stable (that is, $\gamma < \gamma_{\text{thresh}}$). For the intermediate and low-$\beta$ cases, figure 12 shows destabilization with increasing temperature gradient. We believe that the stabilization of high-$\beta$ equilibria is a result of large local negative shear (rightmost panels) that spans over a wide range in $\theta$. The local shear becomes positive only after $\theta_{\text{geo}} > \pi/2$ – the whole outboard side has a large local negative shear. These large negative values are predominantly due to a large Shafranov shift but could have sub-dominant effects resulting from strong shaping, especially for the negative triangularity high-$\beta$ equilibria. For the shifted-circle equilibria, the local shear is small as compared with the rest of the equilibria even though it is negative over the outboard side. This is because the low-$\beta$ shifted-circle equilibria are neither strongly shaped nor have a large beta. The trend remains the same even for the equilibria with half-nominal density gradients. Next, we plot results for negative triangularity equilibria in figure 13.

We see that the high-$\beta$ equilibria with a negative-triangularity boundary shape are stabilized as well. The local magnetic shear shows the same trend with beta but is even more negative and spans an even wider range in $\theta_{\text{geo}}$ as compared with the positive-triangularity equilibria. We believe this extended range in negative local shear is due to the 'squareness' of the high-$\beta$ profiles, which is a stronger shaping than the
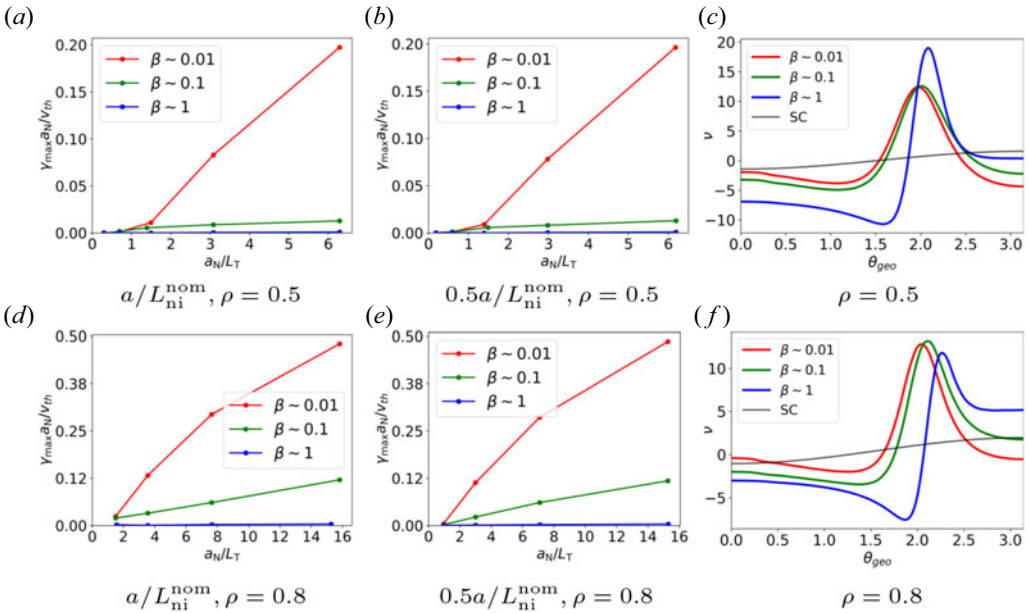
FIGURE 12. This figure shows the ITG $\max(\gamma a_N/v_{\text{th},i})$ plots for positive-triangularity equilibria against the temperature gradient length scale. For the high-$\beta$ equilibria, ITG is stabilized at both $\rho = 0.5$ and $\rho = 0.8$. The rightmost figures in each row are the local magnetic shear vs the geometric theta $\theta_{\text{geo}}$ at the nominal $\mathrm{d}p/\mathrm{d}\rho$ and $\hat{s}$. The grey line corresponds to the local shear for a low-$\beta$ shifted-circle equilibrium (abbreviated SC). The magnetic shear $\hat{s}$ is the same for all the equilibria at every $\rho$.

positive triangularity cases. Since all the high-$\beta$ equilibria are stabilized and the growth rates are small, it is hard to find a clear difference in growth rates based on triangularity.

In the next section, we will study the stability of different equilibria to an electron-driven electrostatic mode, the TEM.

## 6. The TEM study

In this section, we will present our analysis of the TEM instability. In § 6.1, we explain the TEM and tabulate the parameters for which we perform our study. After that, we define the maximum TEM growth rate. In § 6.2, we present the electron precession drift as a characteristic of TEM stability of a local equilibrium. In the final section, we plot the results in a fashion similar to the previous section.

### 6.1. *Details of the study*

The second type of electrostatic instability that we investigate, the collisionless TEM, becomes unstable when drift waves resonate with the precession of the electrons. This can cause significant transport loss through the electron channel that degrades plasma confinement (Adam, Tang & Rutherford 1976). For the TEM, we choose five values of pressure gradient, corresponding to fac $= (0.5, 1, 2, 4, 8)$ for $\rho = 0.5$ and five values corresponding to fac $= (0.5, 0.75, 1, 2, 4)$ for $\rho = 0.8$. For each pressure gradient, we choose two temperature-gradient scale lengths – nominal and 30 % of the nominal, while scanning the growth rates in the density gradient scale lengths. We do this since TEM, unlike ITG, is primarily a density gradient-driven instability. Tables 7 and 8 contain the
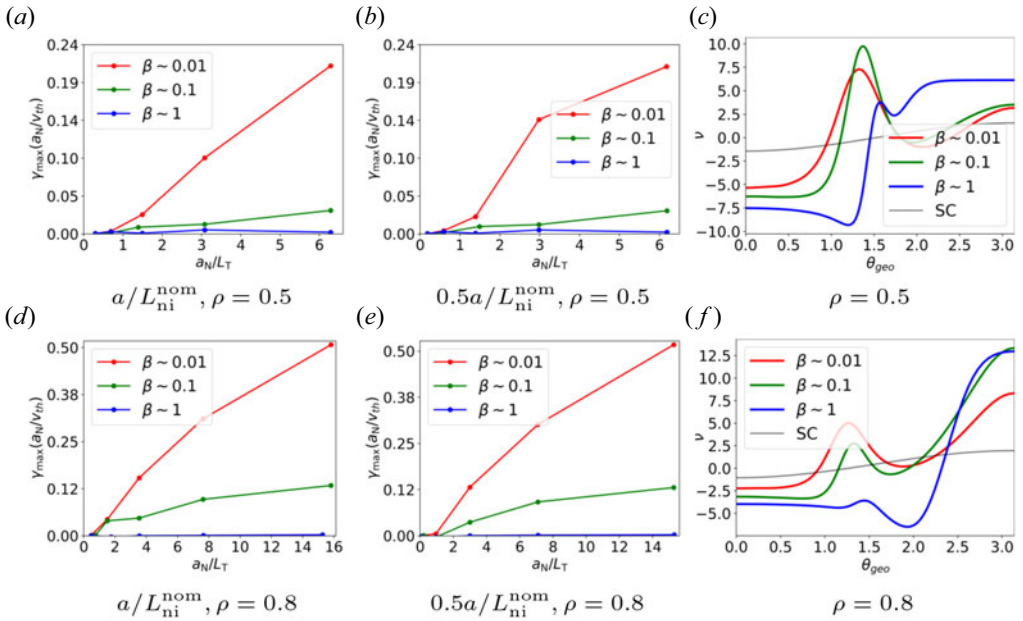
FIGURE 13. Shows the ITG $\max(\gamma a_N/v_{\text{th},i})$ plots for negative-triangularity equilibria. For the high-$\beta$ equilibria, ITG is stabilized at both $\rho = 0.5$ and $\rho = 0.8$. The local shear for the high-$\beta$ equilibria is negative over the whole outboard side. The grey line corresponds to the local shear for a low-$\beta$ shifted-circle equilibrium (abbreviated SC).

| $a_N/L_{T_e} = a_N/L_{T_i}$ | $a_N/L_{n_e} = a_N/L_{n_i}$ | | | | | |
|---|---|---|---|---|---|---|
| 0.186 | 0.21 | 0.61 | 1.41 | 3.01 | 6.22 |
| 0.296 | 0.10 | 0.51 | 1.31 | 2.91 | 6.11 |

TABLE 7. Values of gradient scale lengths at $\rho = 0.5$ used for the TEM study.

| $a_N/L_{T_e} = a_N/L_{T_i}$ | $a_N/L_{n_e} = a_N/L_{n_i}$ | | | | | |
|---|---|---|---|---|---|---|
| 0.95 | 1.09 | 2.11 | 3.13 | 7.22 | 15.45 |
| 1.50 | 0.54 | 1.57 | 2.59 | 6.68 | 14.86 |

TABLE 8. Values of gradient scale lengths at $\rho = 0.8$ used for the TEM study.

values for which we have solved the gyrokinetic model. Note that the temperature and density scale lengths are the same for the ions and electrons.

These 20 values of gradients are the same for ions and electrons as well as both positive- and negative-triangularity equilibria at all the different beta values. Unlike the ITG study, we turn on the kinetic effects of electrons since TEM is an electron-driven instability. The TEM growth rate peak occurs over a wide range $k_y \rho_i \in [0.5, 6]$. Since there is an overlap with the ITG and the electron-temperature-gradient (ETG) mode, having two species makes it difficult to separate modes with purely ITG and ETG-related effects from

modes with purely TEM-related effects. Therefore, to calculate the TEM growth rate, we choose the growth rate corresponding to the wavenumber $k_y\rho_i$ at which the ratio of the quasilinear electron flux to electron heat flux is the maximum, i.e.

$$\gamma_{\text{TEM}}(k_y\rho_i) = \gamma\Big|_{\max(\Gamma_{e,ky}/Q_{e,ky})}, \tag{6.1}$$

where the definition of quasilinear fluxes is given in equations (4.26) and (4.27).

We run GS2 for the wavenumbers in the range $k_y\rho_i \in [0.2, 6.5]$. Just like the ITG study, we run GS2 and obtain the maximum growth rate $\gamma a_N/v_{\text{th},i}$ for each of the 120 cases: 10 values of $(a_N/L_T, a_N/L_n) \times 2$ surfaces $\times 3\ \beta$ values $\times 2$ boundary shapes. The results showing the comparison between different beta values, triangularities, and normalized radius will be shown in § 6.3.

Curvature-driven TEMs are associated with the precession of trapped electrons in a flux surface. To that end, we elucidate the definition and role of the electron precession drift frequency in the next section and how it characterizes the stability of an equilibrium to the TEM.

## 6.2. *Characterizing stability to the TEM*

The collisionless curvature-driven TEM is a drift wave that becomes unstable when it resonates with the bounce precession of trapped electrons. The precession of electrons is characterized by their precession frequency

$$\langle\omega_{\text{De}}\rangle = \left(\int_{-\theta_b}^{\theta_b} \frac{\mathrm{d}\theta}{w_\parallel} \frac{B}{(\boldsymbol{B}\cdot\boldsymbol{\nabla}\theta)}\right)^{-1} \int_{-\theta_b}^{\theta_b} \frac{\mathrm{d}\theta}{w_\parallel} \frac{B}{(\boldsymbol{B}\cdot\boldsymbol{\nabla}\theta)}\omega_{\text{De}}, \tag{6.2}$$

where the integral operator is the bounce-average operator. The precession frequency is a function of the bounce angle $\theta_b$. Depending on the convention, one usually takes $\text{sign}(\omega) = \text{sign}(\omega_{*,e})$ for trapped electron modes since the TEM is a drift wave. Therefore, if

$$\text{sign}(\langle\omega_{\text{De}}\rangle)\text{sign}(\omega_{*,e}) < 0, \tag{6.3}$$

the drift wave will not be able to resonate with the precession of electrons. If the precession drift satisfies (6.3) at all the different pitch angles, the curvature-driven TEM will be stabilized (Connor, Hastie & Martin 1983; Roach, Connor & Janjua 1995). The expression for $\omega_D$, given by (4.20) can be alternatively written as

$$\omega_{\text{De}} = \frac{k_y\rho_e}{2} \frac{v_{\text{th},e}}{a_N} E_e[2(1 - \lambda B)\omega_\kappa + \lambda B\omega_B], \tag{6.4}$$

where $\omega_\kappa(\theta)$ and $\omega_B(\theta)$ are geometric factors independent of the electron energy $E_e$ and the pitch angle $\lambda$. A semi-analytical formula for calculating $\omega_\kappa$ is given in (C29). As a characteristic of TEM stability, we define the quantity

$$\langle\bar{\omega}_{\text{De}}\rangle = \langle\omega_{\text{De}}\rangle\text{sign}(\omega_{*,e})/E_e, \tag{6.5}$$

as the precession drift per energy in the electron diamagnetic direction. A typical plot of the $\langle\bar{\omega}_{\text{De}}\rangle$ is shown at nominal $\hat{s}$ and $\alpha_{\text{MHD}}$ for different $\beta$ values in figure 14. We see that the precession drift is negative everywhere only for high-$\beta$ case. This will form the basis for our understanding of the growth rate trends in the following section.
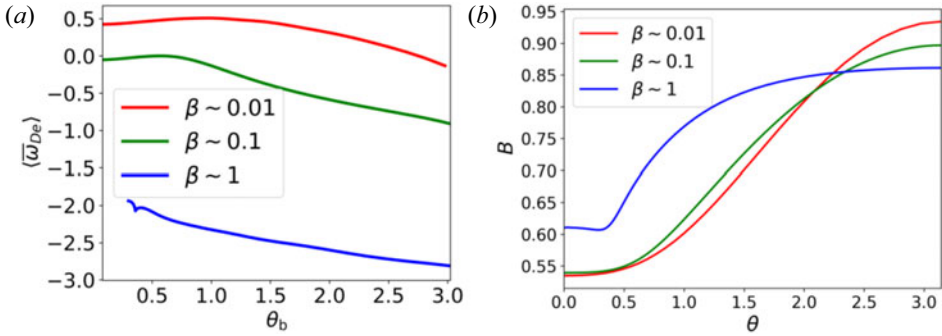
FIGURE 14. This figure shows the precession drift in (*a*) and the corresponding magnetic field magnitude in (*b*) for negative-triangularity equilibria at $\hat{s} = 0.45$ and nominal $\alpha_{\text{MHD}}$ values at $\rho = 0.8$ for different beta values. Note the atypical magnetic field for the high-$\beta$ equilibria where $\min(B)$ is located at a finite $\theta$.
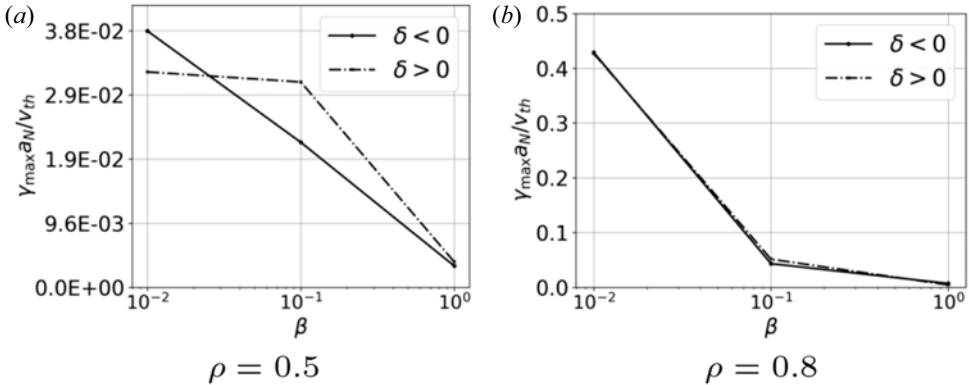


FIGURE 15. This figure shows the TEM $\gamma_{\text{TEM}}(a_N/v_{\text{th},i})$ vs the typical $\beta$ plots for nominal equilibria at different radial locations.

### 6.3. *The TEM results*

Just like the ITG study, we choose a value of a growth rate $\gamma_{\text{thresh}}$ such that if $\gamma_{\text{TEM}}(a_N/v_{\text{th},i}) < \gamma_{\text{thresh}}$, we classify an equilibrium as stable. The reasoning behind setting a threshold is described in the first paragraph of § 5.3. For this study, we choose $\gamma_{\text{thresh}} = 0.005$. First, we plot the maximum TEM growth rates for the nominal equilibria in figure 15. We find that increasing the beta stabilizes the TEM and the high-$\beta$ equilibria are stable to the TEM.

To understand this effect further, we plot the result from scans in the density gradients in two groups, each group containing the maximum TEM growth rate for a range of $a/L_n$ at a fixed $a/L_T$, given in tables 7 and 8 for different equilibria. Just like the ITG study, we group the plots by triangularity and arrange them in rows based on the normalized radius $\rho$. For positive triangularity equilibria, the results are shown in figure 16

We observe that the TEM is completely suppressed for the high-$\beta$, positive-triangularity equilibria. The frequency $\langle \bar{\omega}_{\text{De}} \rangle$ is negative everywhere which means that all the trapped electrons precess in a direction opposite to the electron diamagnetic direction. They cannot destabilize the drift wave by exchanging energy with them.
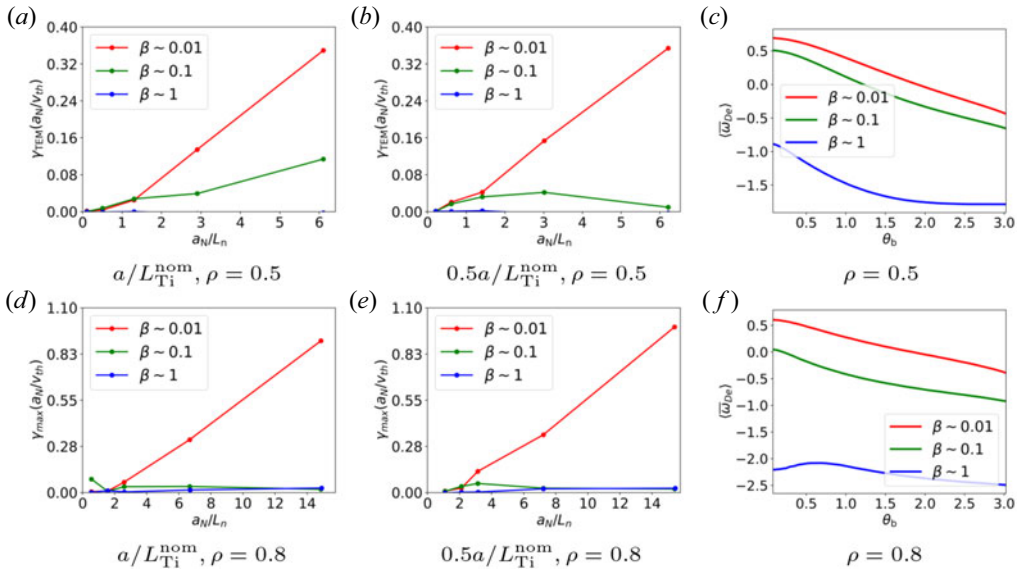
FIGURE 16. This figure presents $\gamma_{\text{TEM}}(a_N/v_{\text{th},i})$ plots for positive-triangularity equilibria. For the high-$\beta$ equilibria, TEM is stabilized at both $\rho = 0.5$ and $\rho = 0.8$. As you can see in figures 19(c) and 19(f), the precession drift for the high-$\beta$ equilibria is negative for all values of the bounce angle $\theta_b$.

The TEMs we seek are curvature driven. A large pressure gradient causes the electron precession drift to become negative for all pitch angles (Roach *et al.* 1995). This suppresses the curvature-driven mode and causes the slab-like branch of the TEM called the universal mode to appear. We can see that the universal mode dominates in figures 16(b) and 17(b) for the intermediate-$\beta$ equilibria at large density gradients. However, for high-$\beta$ equilibria, the universal mode is suppressed as well since the large local shear

$$L_v = \frac{a_N}{v}, \qquad (6.6)$$

combined with strong shaping reduces the shearing length scale (Landreman, Antonsen & Dorland 2015) which makes it harder for fluctuations to grow and persist along the field line.

Next, now look at the TEM growth rate trends for the negative triangularity equilibria, shown in figure 17. The negative-triangularity TEM growth rates follow the same trend as the positive-triangularity ones. The TEM is suppressed for the high-beta equilibria due to the negative precession drift. The intermediate and low beta are more unstable for thenegative-triangularity equilibria at $\rho = 0.5$ and as unstable as the positive-triangularity ones at $\rho = 0.8$.

The result of our local analyses are only strictly valid for perturbations localized to a field line on a flux surface. Alternatively, one can say that for all the fluctuations, the toroidal mode number $n \gg 1$. Therefore, we must ensure that all modes in this study meet the local approximation in order to ensure that they are self-consistent. In both § 5 and § 6, the lowest wavenumber in our analyses is $k_y \rho_i = 0.05$. The largest ion gyroradius arises in the outer-core high-$\beta$ equilibria where $\rho_i \approx 0.005$ m. This corresponds to a wavelength $\lambda = 0.628$ m. Assuming an $n = 1$ mode has a wavelength equal to the normalized minor radius $a_N = 0.68$ m, $k_y \rho_i = 0.05$ corresponds to $n \approx 1$ – the longest modes are not
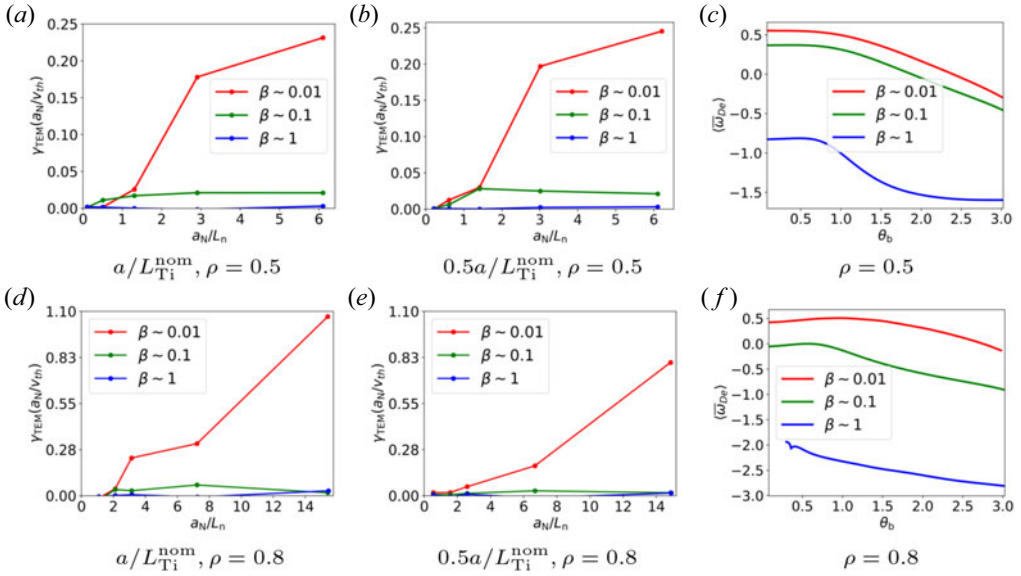
FIGURE 17. This figure presents $\gamma_{\mathrm{TEM}}(a_N/v_{\mathrm{th},i})$ plots for negative-triangularity equilibria. For the high-$\beta$ equilibria, TEM is stabilized at both $\rho = 0.5$ and $\rho = 0.8$. The rightmost plot on each row is the electron precession drift frequency.

localized. Hence, to accurately capture these modes at low wavenumbers, we must include non-local effects. However, for all the electrostatic studies, the growth rates $\gamma a_N/v_{\mathrm{th},i} \to 0$ as $k_y\rho_i \to 0$ and the most unstable modes always arise at $k_{y,\mathrm{peak}}\rho_i \geq 0.5$ which corresponds to $n \geq 10$ implying that the local approximation is a fair assumption since we are only concerned with peak growth rates in §§ 5 and 6.

We have demonstrated the stability of high-$\beta$ equilibria against two major sources of electrostatic instabilities. However, when $\beta \sim 1$, magnetic fluctuations may play an important role in deciding the stability of an equilibrium. Therefore, in the next section, we study the effect of electromagnetic modes on the high-$\beta$ equilibria.

## 7. Linear electromagnetic study

To see if the stability trend seen in the electrostatic study holds when we include electromagnetic effects, we perform an electromagnetic microstability analysis for all the nominal local equilibria. This analysis is similar to the work done by Belli & Candy (2010), albeit we are testing $\beta \sim 1$ equilibria using an initial-value solver. We solve the linear, collisionless, gyrokinetic model allowing for non-zero magnetic field perturbations $\delta A_\parallel$ and $\delta B_\parallel$ using the GS2 code. We use the nominal gradient scale lengths for this study (given in table 4). First, we plot the growth rate spectrum with $k_y\rho_i$ for the positive-triangularity cases in figure 18.

Since GS2 only calculates the maximum growth rate, in the inner core, we observe the finite-$\beta$ stabilization of ITG (Candy & Waltz 2003b) until the emergence of collisionless-microtearing (MTM) (Kotschenreuther *et al.* 1995a; Guttenfelder *et al.* 2011; Dickinson *et al.* 2013) and electromagnetic-ETG (EM-ETG) modes (Kim & Horton 1991; Joiner & Hirose 2007) in figure 18(c)[11] . These modes arise on small scales radially

---

[11]Note that the purpose of this work is to look for the most unstable modes destabilizing a local equilibrium. The distinction and correct classification of the type of mode is orthogonal to our objectives.
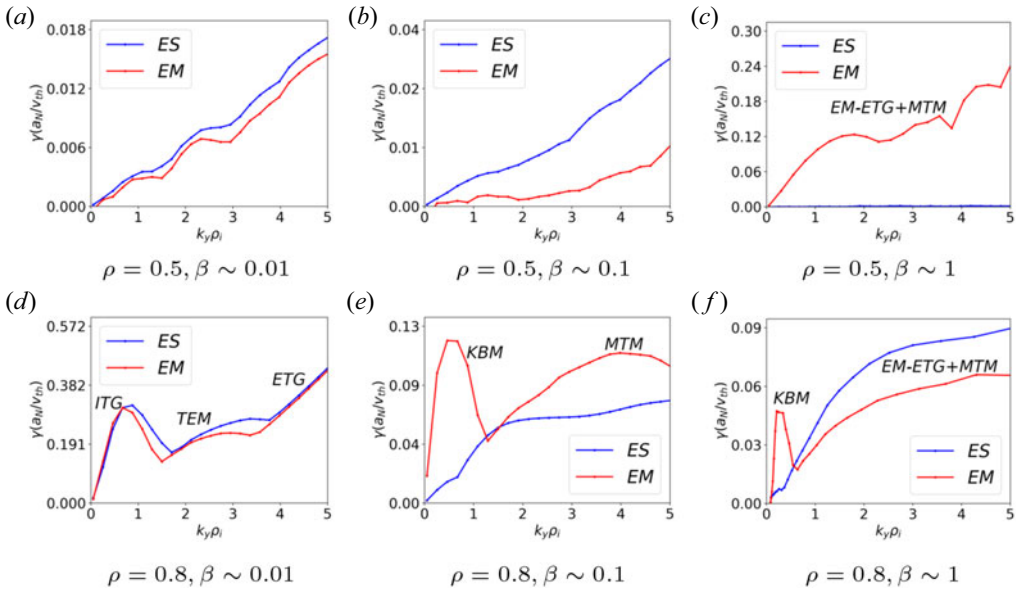
FIGURE 18. This figure shows comparison between the electrostatic (abbreviated ES) and electromagnetic (abbreviated EM) growth rates for all the nominal positive-triangularity equilibria. Some of the branches have been labelled by their corresponding mode names. Notice the KBM in the intermediate and high-$\beta$ equilibria in figures 21($e$) and 21($f$), respectively and the emergence of the collisionless-microtearing and electromagnetic-ETG modes in figure 21($c$) for all values of $k_y\rho_i$ and figures 21($e$) and 21($f$) for $k_y\rho_i > 1$.

($O(\rho_e)$) and are extended in the ballooning angle $\theta$. To accurately capture the extended eigenfunctions corresponding to these modes, we have to choose a wide range in the field-line-following coordinate ($\theta \in [-119\pi, 119\pi]$) with 21 points over a $2\pi$ interval. The eigenfunctions for two values of $k_y\rho_i$ in figure 19($c$) are shown in figure 24 in Appendix E.

In the outer core, we observe finite-$\beta$ stabilization only for the low-$\beta$ equilibrium. For the intermediate and high-$\beta$ cases, the electrostatic modes are replaced by kinetic ballooning modes (KBMs) at low wavenumbers and collisionless-MTM and EM-ETG at high wavenumbers. Overall, positive-triangularity high-$\beta$ equilibria are more unstable than the low or intermediate ones in the inner core due to the collisionless-MTM and the EM-ETG mode. As we move towards the outer core, high-$\beta$ equilibria become much more stable – exactly the opposite trend compared with the inner core. This means that the outer core is more stable for the high-$\beta$ equilibria.

Next, we plot the growth rates for the negative-triangularity equilibria in figure 19. The negative-triangularity, inner-core equilibria are also stabilized due to finite-$\beta$ effects. This effect is also visible for the intermediate-$\beta$ case for $k_y\rho_i > 0.5$ but absent for the high-$\beta$ cases as the ITG and TEM are superseded by electromagnetic modes: collisionless-MTM and the EM-ETG mode. For the outer-core cases, we see the exact same pattern as the inner core – finite-$\beta$ stabilization for the low-$\beta$, KBM and collisionless-MTMs for the intermediate-$\beta$ and collisionless-MTMs and EM-ETG modes for the high-$\beta$. Note that unlike the positive-triangularity case, we do not observe the KBM in the negative-triangularity, high-$\beta$ equilibria. Moreover, the growth rates are also smaller than the positive triangularity cases for a wide range of wavenumbers ($k_y\rho_i \in [0.01, 4.5]$). Since
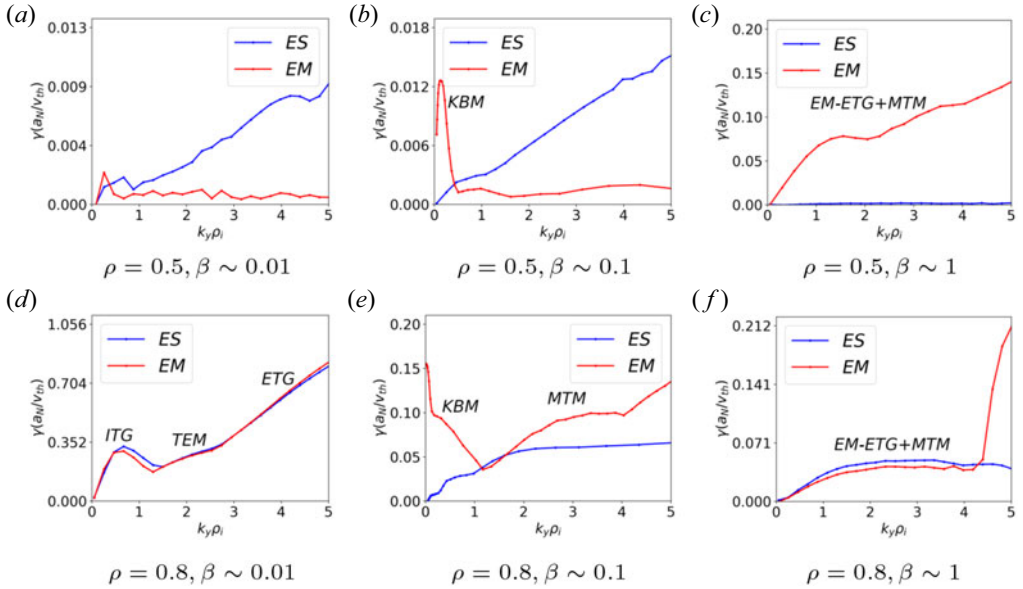
FIGURE 19. This figure shows comparison between the electrostatic (ES) electromagnetic (EM) growth rates for all the nominal negative triangularity equilibria. The sudden jump in figure 19($f$) around $k_y \rho_i = 4.5$ is a different branch of the collisionless MTM. Note also that the growth rate around $k_y \rho_i = 0$ in figure 19($e$) goes to fixed value of $\gamma a_N / v_{\text{th},i} = 0.152$ since the equilibrium is unstable to the ideal-ballooning mode.

turbulence is most likely to peak at lower wavenumbers, the growth rate characteristics of negative-triangularity, high-$\beta$ are the most favourable.[12]

In summary, we find that turning on the electromagnetic effects destabilizes the high-$\beta$ equilibria. Figures 18($c$), 19($c$) and 19($f$) show the emergence of collisionless-MTMs and EM-ETG modes whereas figure 18($c$) also shows instability to the KBM in the range $k_y \rho_i \in [0.01, 0.5]$. These equilibria are much more unstable than the low-$\beta$ ones in the inner core but they are much more stable as we move towards the outer core, with negative-triangularity high-$\beta$ equilibria showing the best characteristics. We believe that the outer-core stability is due to a large Shafranov shift and strong shaping. We also argue that negative triangularity has better characteristics than positive triangularity due to stronger shaping, i.e. 'squareness' that we discussed in figure 3. It is also interesting to note that for the negative-triangularity equilibria, the growth rate trend matches that of the ideal-ballooning stability in figure 6 – less stable towards the core, more stable towards the edge. Since outer-core or edge transport is usually a limiting factor in experimental low-$\beta$ equilibria, these equilibria may be a novel alternative to realize higher-power devices.

In this section, the lowest wavenumber that we have scanned is $k_y \rho_i = 0.01$. Using the same analyses as presented at the end of § 6, the longest wavelength $\lambda \approx 3.1$m. Assuming $n = 1$ corresponds to $\lambda = a_N = 0.68$ m, the longest mode would require $n < 1$. Modes with such long wavelengths violate the local assumption of flux tube codes. However, the

---

[12]Some of the $\beta \sim 1$ equilibria have small but finite TEM growth rates which are larger than the growth rates from our electrostatic TEM study. This is consistent with the electrostatic study since we chose the TEM growth rate at a value of $k_y \rho_i$ for which the ratio of $\Gamma_e / Q$ was maximized. This almost always happens at a low $k_y \rho_i$ – TEM growth rates are small at low $k_y \rho_i$ values for $\beta \sim 1$. Moreover, the values of the gradient scale lengths (tables 7 and 8) were different for the electrostatic study.

growth rates go to zero at low wavenumbers (with the exception of figure 19*e*) and peak at $k_{y,\text{peak}}\rho_i \gg 0.01$. Calculating the value of $n$ at the wavenumber $k_{\text{peak}}\rho_i$, we obtain the lowest $n$ in figures 19(*e*) and 18(*f*) as $n = 0$ and $n = 5$, respectively. Therefore, the reader must take the low-wavenumber results shown in figures 19(*e*) and 18(*f*) with a grain of salt.

Note that this is a collisionless electromagnetic analysis. It is possible that in the presence of collisions, more modes like collisional-MTMs (Applegate *et al.* 2007; Patel *et al.* 2021), collisional EM-ETG etc. arise and supersede their collisionless variants (Dickinson *et al.* 2013) as the most dominant mode. On the other hand, it is also possible to achieve lower growth rates if we include the stabilizing effect of velocity shear (Patel *et al.* 2021).

## 8. Summary and conclusions

We began this work by deriving the Grad–Shafranov equation and briefly discussed existing approaches used to obtain $\beta \sim 1$ axisymmetric equilibria in § 2. In § 2.1, we generated numerical high-$\beta$ equilibria using the 3-D equilibrium code VMEC. We produced different equilibria based for three beta values: low, intermediate and high ($\beta \sim 1$), each differing from the rest by at least an order or magnitude. We also chose two different boundary shapes with negative and positive triangularity. For each global equilibrium, we picked two local equilibria: one in the inner core and the other in the outer core. This gave us a total of 12 local equilibria.

Upon ensuring that these equilibria are smooth and well resolved, we first tested their stability against the infinite-$n$ ideal-ballooning mode in § 3. Since the ideal-ballooning mode is an MHD instability, we chose the local equilibria such that all the high and low-$\beta$ equilibria are ideal-ballooning stable. We also elucidated the idea of varying the magnetic shear and pressure gradient self-consistently, the Greene–Chance analysis in § 3.2. This powerful technique enabled us to know how far the local equilibria are from the region of marginal stability.

In § 4, we briefly explained the linear, collisionless, gyrokinetic model. In §§ 5 and 6, we use this to study the stability of all the local equilibria to the two most virulent electrostatic modes of turbulence: ITG and TEM. We found a clear inverse relationship between the beta value and the growth rates – increasing the beta value stabilized both the ITG mode and the TEM. Using a Greene–Chance analysis, we also scanned the maximum ITG, TEM growth rates vs the temperature and density gradient scale lengths, respectively. This was important to ensure that these equilibria are not 'stiff', i.e. the growth rates do not increase sharply as the gradients exceed some threshold. In § 5.2, we explained how a large negative local shear resulting from a large Shafranov shift stabilizes the ITG mode and in § 6.2 we showed how the reversal of the precession of the trapped electrons stabilizes the TEM throughout the whole range of gradient scale lengths.

The effect of electromagnetic fluctuations can be important for all equilibria, especially the intermediate and high-$\beta$ ones. To that end, in § 7 we performed an electromagnetic study of all the nominal equilibria. We found that the stability trend seen for the electrostatic case did not hold after turning on electromagnetic effects. However, even though the high-$\beta$ equilibria were more unstable than the low-$\beta$ ones due to collisionless-MTMs and EM-ETGs in the inner core, they were much more stable than low-$\beta$ in the outer core. We found that negative-triangularity, high-$\beta$ equilibria were stable to the KBM. We believe that this is due to the strong shaping ('squareness') of the negative-triangularity high-$\beta$ equilibria. This indicates that turbulent transport may flatten the pressure gradient in the core but may not significantly affect the pressure gradient toward the edge for high-$\beta$ equilibria.

This work suggests many promising avenues for future research. One could repeat the same study with a wider range of input parameters to determine whether the microstability trends we have found are not strongly dependent on the input parameters. An important path to explore would be to map the trajectory of these high-$\beta$ equilibria, starting from a low-beta equilibrium in the $\hat{s} - \alpha_{\mathrm{MHD}}$ space such that it is always stable to major sources of disruption. This would guarantee a high-$\beta$ operation free from any ideal-MHD instability. Once such a path is found, the final step would be to do a microstability calculation scan for different values of collisionalities followed by a transport calculation to obtain the evolution of the density and temperature profiles.

### Declaration of interest

The authors report no conflict of interest.

### Data availability statement

The VMEC and GS2 input files as well as the helper scripts used for creating various plots are available here.

### Appendix A. Hsu, Artun and Cowley's analytical ($\beta \sim 1$) equilibrium

In this appendix, we provide a brief overview of the analytical, high-$\beta$ equilibrium derived by Hsu, Artun and Cowley. In § A.1, we describe the asymptotic ordering and the procedure used to analytically solve the Grad–Shafranov equation for $\beta \sim 1$. In § A.2, we discuss two major limitations of these analytical solutions in the context of local stability analyses.

### A.1. *Generating analytical $\beta \sim 1$ equilibria*

The most general analytical theory for generating $\beta \sim 1$ equilibria was first developed by Hsu, Artun, and Cowley (Hsu *et al.* 1996). In that work, the Grad–Shafranov equation is solved analytically in the limit

$$\delta_{\mathrm{Hsu}} \equiv \sqrt{\epsilon/(\beta q^2)} \ll 1, \tag{A1}$$

where $\epsilon = a/R_0$ is the aspect ratio of the flux surface – $a$ being the minor radius of a flux surface and $R_0$ being the major radius. For these equilibria, it is assumed $B_t/B_p \sim q/\epsilon$ where $B_t = \boldsymbol{B} \cdot \nabla\phi/|\nabla\phi|$, $B_p = \boldsymbol{B} \cdot \nabla\theta/|\nabla\theta|$ are the toroidal and poloidal components of the magnetic field, respectively, and $\epsilon \sim \beta \sim 1$ on all surfaces of interest.

Given these assumptions, Hsu *et al.* solve the Grad–Shafranov equation to calculate the perpendicular distance from the boundary to a point on the flux surface labelled $\psi$

$$\xi = \int_{R_{\min}}^{\hat{R}'} \frac{(\mathrm{d}\psi/\mathrm{d}\hat{R}')\,\mathrm{d}\hat{R}'}{\sqrt{\int_{R}^{\hat{R}'} \mu_0(\hat{R}''^2 - R^2)\dfrac{\mathrm{d}p}{\mathrm{d}\hat{R}''}\,\mathrm{d}\hat{R}''}}, \tag{A2}$$

where $\hat{R}(\psi)$ is the value of $R$ on the line $Z = 0$ and $p$ is the plasma pressure. Using $\xi$, they formulate the 'core' solution, i.e. the solution on the inboard side where the surfaces are nearly vertical

$$Z(\hat{R}, R) = l(R) - \frac{\xi(\hat{R}, R)}{\cos(\theta_s)}, \quad \theta_s = \arctan\left(\frac{\mathrm{d}l}{\mathrm{d}Z}\right), \tag{A3}$$

and the 'boundary layer' solution, i.e. the solution in the region of closely spaced surfaces on the outboard side

$$R_{\text{boundary}}(Z) = R(\hat{R}, Z) + \frac{\xi(\hat{R}, R_{\text{boundary}})}{\sin(\theta_s)}, \tag{A4}$$

where $l = l(R)$ in (A3) is the value of $Z$ on a point on the boundary. To construct a $\beta \sim 1$ equilibrium, one needs an analytical pressure, boundary shape profiles and the value of the poloidal field at $Z = 0$. Hsu *et al.* used the following profiles:

$$\left.\begin{aligned}
p(\hat{R}(\psi)) &= p_1\left(1 - \frac{p_2(R_{\max} - \hat{R})^2 + p_3(R_{\max} - \hat{R})^3 + p_4(R_{\max} - \hat{R})^4}{p_2(R_{\max} - R_{\min})^2 + p_3(R_{\max} - R_{\min})^3 + p_4(R_{\max} - R_{\min})^4}\right), \\
l_{\delta<0}(\hat{R}) &= (\hat{R} - R_{\min})^{0.5}(R_{\max} - \hat{R})^{0.5}\left(\frac{a_l}{[R_{\max} - R + b_l(R_{\max} - R_{\min})]^{c_l}}\right)^{0.5}, \\
\frac{1}{\hat{R}}\frac{\mathrm{d}\psi}{\mathrm{d}\hat{R}} &= \frac{l(\hat{R})}{\hat{R}}[a_\psi + b_\psi(\hat{R} - R_{\min}) + c_\psi(\hat{R} - R_{\min})^2],
\end{aligned}\right\} \tag{A5}$$

where $l_{\delta<0}$ is a function used to generate the boundary shapes corresponding to a negative-triangularity equilibria. After fixing the various input profiles, one solves (A2) to obtain the perpendicular distance $\xi$ as a function of $\hat{R}$ and $R$. Substituting $\xi$ in (A3) and (A4), one gets the core and boundary layer segments, respectively. Taking union of the two segments yields the flux surface contour $\psi(R, \hat{R})$. Figure 20 illustrates this process.

## A.2. *Limitations of the Hsu et al. equilibria*

We find that the equilibria of Hsu *et al.* has two major limitations that can significantly affect the accuracy of our analyses. First, as we move closer to the magnetic axis, the accuracy of both the core and boundary layer solution degrades as the ordering $\epsilon \sim 1$ fails and $\mathrm{d}p/\mathrm{d}\psi$ approaches zero. We demonstrate this by plotting figure 21 which is figure 6
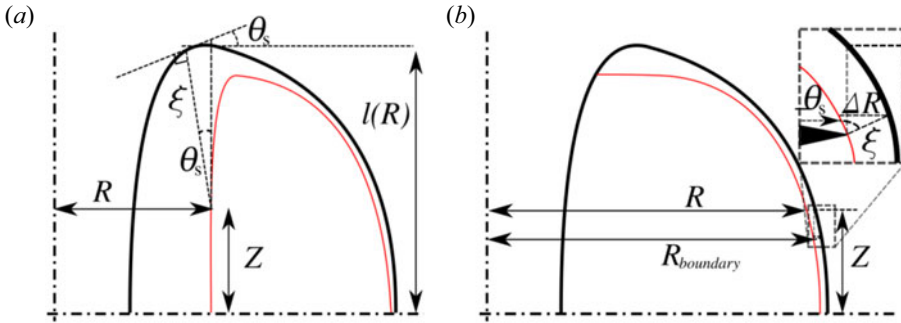
FIGURE 20. This figure illustrates the process of creating the two regions of the $\beta \sim 1$ solution in Hsu *et al.* The bold black line is the LCFS and red line is the flux surface contour – (*a*) shows the core solution (A3) which is only a good approximation on the inboard side of the device and (*b*) shows the boundary layer solution (A4) which is only valid in the boundary layer region. The inset in the right figure highlights the approximation $\xi(\hat{R}, R) = \xi(\hat{R}, R_{boundary})$ which is necessary to construction the boundary layer solution (A4).
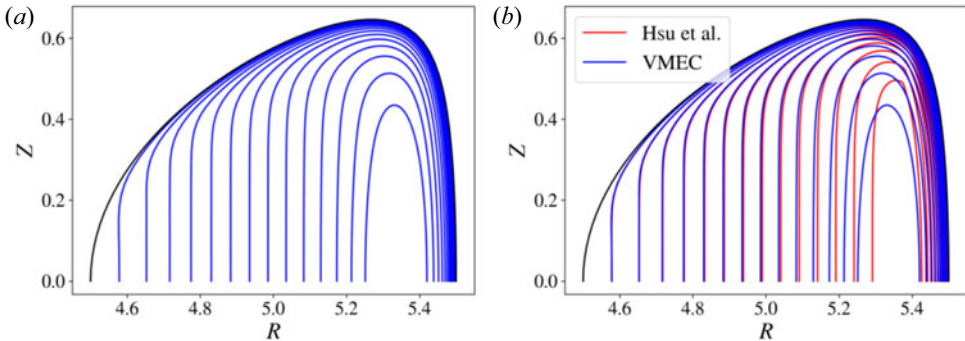


FIGURE 21. This figure shows (*a*) the numerical equilibrium solution and (*b*) a comparison between the analytical equilibrium from figure 6 in the paper by Hsu *et al.* and the same equilibrium generated using VMEC. We can clearly see the significant deviation of the analytical solution and how it develops a kink near the outboard side as we approach the magnetic axis.

in Hsu *et al.* To generate the analytical solution in figure 21, we start with (A5) using the following values of coefficients:

$$
\left.
\begin{aligned}
(p_1, p_2, p_3, p_4) &= (0.5, 1.5, 0, 0), \\
(a_l, b_l, c_l) &= (0.8, 0.05, 0.85), \\
(a_\psi, b_\psi, c_\psi) &= (0.152, 0.022, 0).
\end{aligned}
\right\}
\tag{A6}
$$

Secondly, the inaccuracy and non-smoothness of flux surfaces leads to discontinuous and incorrect trends in the geometric quantities needed for a local stability analysis. To demonstrate this, we plot a physical quantity that arises in both the ballooning and gyrokinetic equation that can be seen in (3.3) and (4.17) in §§ 3 and 4, respectively – as a curvature drive in the former and as a component of the curvature drift in the latter. We chose to plot the scalar

$$
\hat{\kappa} = \frac{1}{B^3}(\boldsymbol{b} \times \boldsymbol{\kappa}) \cdot \nabla\alpha, \quad \boldsymbol{\kappa} = (\boldsymbol{b} \cdot \nabla\boldsymbol{b}),
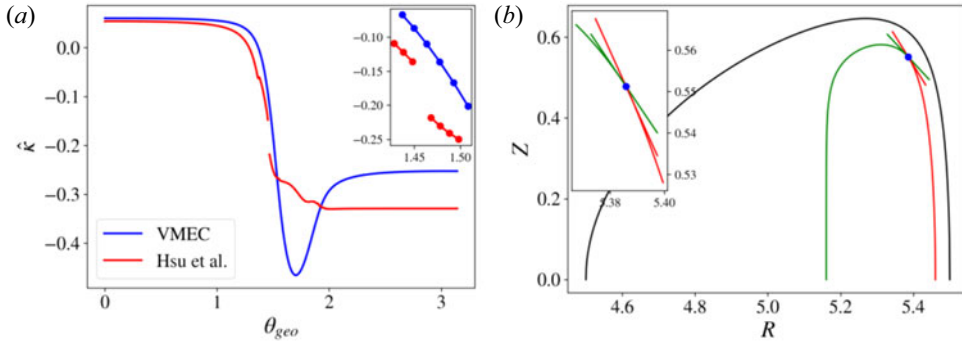\tag{A7}
$$

FIGURE 22. In this figure (*a*) compares $\hat{\kappa}$ vs. $\theta_{geo}$ obtained using the analytical equilibrium(in figure 6) in Hsu *et al.* with the corresponding VMEC equilibrium for a common flux surface(shown in (*b*)). The inset in (*a*) shows a zoomed-in version of the same plot near the discontinuity at $\theta_{geo} = 1.46$. Panel (*b*) shows the difference in slopes of the tangents at the point of discontinuity, with a zoomed-in version in the inset. Notice also the deviation of $\hat{\kappa}$ in (*a*) for $\theta_{geo} > 1.5$. There are other issues like the small sharp feature near $\theta_{geo} = 1.3$ that we will not delve into.

where $\kappa$ is the field-line curvature. To better understand the discontinuity problem, we plot $\hat{\kappa}$ as a function of $\theta_{geo}$ in figure 22. To emphasize the importance of smoothness, we also plot the tangents on the flux surface on either side of the point at which $\hat{\kappa}$ is discontinuous. The kink in $\psi$ seen in figure 4(*b*) manifests itself as a discontinuity in quantities like $\boldsymbol{b}$, $\nabla\psi$ and $\nabla\alpha$. This causes the geometric factors, and hence the physical quantities needed for a local stability analysis to become discontinuous. Furthermore, in the regions where the gradients are continuous, for reasons mentioned at the beginning of this section, the distances between the surfaces deviate from the exact equilibrium, especially as $\theta_{geo} > 1.5$. To alleviate these problems, we use the numerical solver VMEC to create the equilibria used in this study.

## Appendix B. Straight-field-line $\theta$ calculation

We briefly describe the process of calculating the straight-field-line $\theta$. We start with the angle $\theta_{geo}$ which is be the geometric angle of a point on a flux surface measured about the magnetic axis and perform this analysis at a fixed toroidal angle $\phi$. We also assume that we know the various Jacobians $\mathcal{J}_{geo} = (\boldsymbol{B} \cdot \nabla\theta_{geo})^{-1}$ and $\mathcal{J} = (\boldsymbol{B} \cdot \nabla\theta)^{-1}$. The transformation relation will then be

$$\theta = \theta_{geo} - \tilde{\nu}(\psi, \theta_{geo}), \tag{B1}$$

where $\tilde{\nu}$ is a periodic function of $\theta_{geo}$ and $\theta$ and $\tilde{\nu}(\psi, \pm\pi) = 0$ for consistency. Applying the $\boldsymbol{B} \cdot \nabla$ operator

$$\boldsymbol{B} \cdot \nabla\theta = \boldsymbol{B} \cdot \nabla\theta_{geo} - \boldsymbol{B} \cdot \nabla\tilde{\nu}. \tag{B2}$$

A special property of the straight-field-line theta is that $q(\psi) = \boldsymbol{B} \cdot \nabla\phi / \boldsymbol{B} \cdot \nabla\theta$. This implies $\boldsymbol{B} \cdot \nabla\theta = F/qR^2$. Using this and dividing (B2) by $\boldsymbol{B} \cdot \nabla\theta$ and integrating in $\theta_{geo}$ from $-\pi$ to $\theta_{geo}$

$$\left.\begin{aligned}
\tilde{\nu}(\theta_{geo}) &= \theta_{geo} - \int_{-\pi}^{\theta_{geo}} \frac{qR^2}{F\mathcal{J}_{geo}} \, d\theta, \\
\theta &= \int_{-\pi}^{\theta_{geo}} \frac{qR^2}{F\mathcal{J}_{geo}} \, d\theta.
\end{aligned}\right\} \tag{B3}$$

Since all the equilibria we are studying are up–down symmetric, we can also assert $\tilde{\nu}(\psi, -\theta_{\mathrm{geo}}) = -\tilde{\nu}(\psi, \theta_{\mathrm{geo}})$ which means $\tilde{\nu}(\psi, 0) = 0$ and

$$\theta = \int_0^{\theta_{\mathrm{geo}}} \frac{qR^2}{F\mathcal{J}_{\mathrm{geo}}} \, \mathrm{d}\theta. \tag{B4}$$

## Appendix C. Greene–Chance's method

This appendix explains the Greene–Chance method, a powerful technique that allows one to vary the pressure and current gradients for a local equilibrium. We will start by defining the local coordinate system first developed by Mercier & Luc (1974). After that, we will expand the Grad–Shafranov equation in those coordinates and use it to obtain other important relations, namely the gradients of $q$, $B$ and $\alpha$ around a surface. Finally, we explain how the derived relations can be used to vary a local equilibrium. All the lengths in the following calculations are normalized using $a_N$ and the magnetic fields using $B_N$. In Appendices C.1 and C.2, we define $\rho$ to be the normalized radial distance from a flux surface whereas in Appendix C.3 $\rho$ is a normalized flux surface label – exactly the same quantity as used in the main body of this work.

### C.1. *Mercier–Luc local coordinate system*

The Mercier–Luc (ML) coordinate system is a local orthogonal coordinate system $(\rho, \phi, l_p)$ where $\rho$ is the normalized perpendicular distance from a point on the flux surface, $\phi$ is the cylindrical azimuthal angle, and $l_p$ is the normalized poloidal arc-length. In these local coordinates we can write, the cylindrical $(R, \phi, Z)$ coordinates as

$$\left.\begin{aligned}
R &= R_0 + \rho \sin(u(l_p)) + \int_0^{l_p} \cos(u) \, dl'_p, \\
Z &= Z_0 + \rho \cos(u(l_p)) + \int_0^{l_p} \sin(u) \, dl'_p,
\end{aligned}\right\} \tag{C1}$$

where $R_0, Z_0$ are the normalized $R, Z$ values on the outboard mid-plane of the flux surface of interest and the angle $u$ is defined as shown in figure 23. We also define

$$\left.\begin{aligned}
R_s &\equiv R(\rho = 0, l_p) = R_0 + \int_0^{l_p} \cos(u) dl'_p, \\
Z_s &\equiv Z(\rho = 0, l_p) = Z_0 + \int_0^{l_p} \sin(u) dl'_p,
\end{aligned}\right\} \tag{C2}$$

as the on-surface cylindrical coordinates. The azimuthal angle $\phi$ is the same for both cylindrical and ML coordinates. Using (C1) and after choosing a sign for the curvature, we can define the curvature

$$\frac{1}{R_c} = \frac{\mathrm{d}u}{\mathrm{d}l_p}, \tag{C3}$$

where $R_c$ is the radius of curvature. Using the coordinate transformation relation (C1), we can write

$$\begin{bmatrix} \mathrm{d}R \\ \mathrm{d}\phi \\ \mathrm{d}Z \end{bmatrix} = \begin{bmatrix} \sin(u) & 0 & \left(1 + \dfrac{\rho}{R_c}\right)\cos(u) \\ 0 & 1 & 0 \\ -\cos(u) & 0 & \left(1 + \dfrac{\rho}{R_c}\right)\sin(u) \end{bmatrix} \begin{bmatrix} \mathrm{d}\rho \\ \mathrm{d}\phi \\ \mathrm{d}l_p \end{bmatrix}. \tag{C4}$$
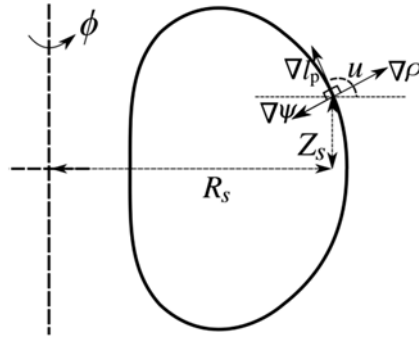
FIGURE 23. This figure illustrates the local orthogonal coordinate system $(\rho, \phi, l_p)$. The radial distance $\rho$ is measured in the direction normal to a flux surface and poloidal arc length $l_p$ is measured in a counter-clockwise sense from the outboard side. We choose $\nabla\psi$ to point in the direction opposite to $\nabla\rho$.
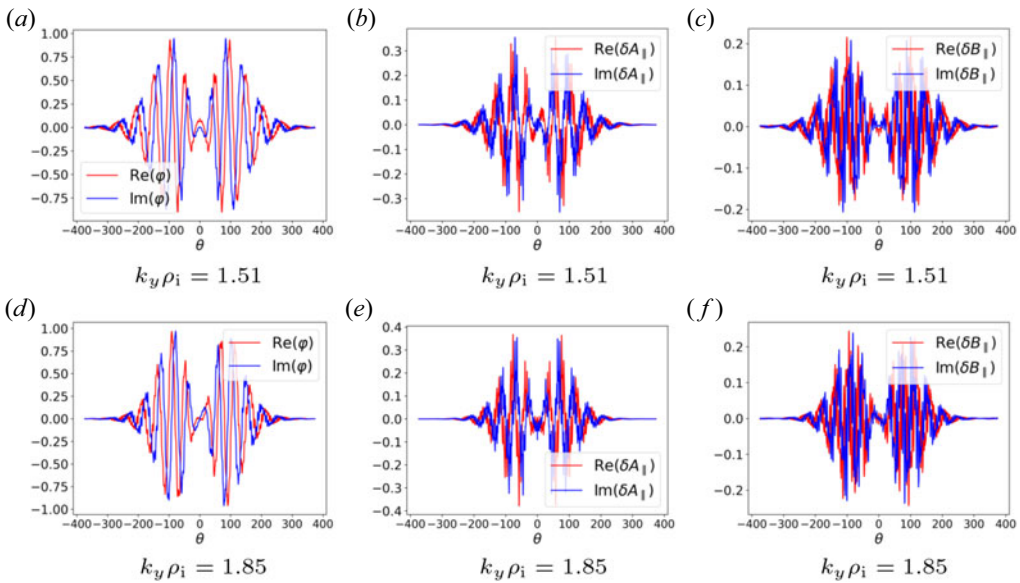


FIGURE 24. This figure shows the eigenfunctions at two different $k_y\rho_i$ values from figure 22(c). The values in each row have been normalized with $\max(\varphi)$. Notice the opposite parities of the eigenfunctions in the two rows and the extended and highly oscillatory structure along $\theta$. The eigenfunctions in the upper row correspond to a non-tearing-parity EM-ETG mode whereas the lower row corresponds to a tearing-parity EM-ETG mode. Classifying modes becomes harder for up–down asymmetric equilibria and virtually impossible for nonlinear analyses.

This matrix can be inverted to obtain the transformation from ML to cylindrical coordinates. Using this transformation, we can write the transformation Jacobian

$$\tilde{\mathcal{J}} = ((\nabla\rho \times \nabla\phi) \cdot \nabla l_p)^{-1} = R\left(1 + \frac{\rho}{R_c}\right). \tag{C5}$$

### C.2. *Expanding the Grad–Shafranov equation locally*

The Grad–Shafranov equation

$$R^2 \nabla \cdot \left( \frac{\nabla \psi}{R^2} \right) = -R^2 \frac{\mathrm{d}p}{\mathrm{d}\psi} - F \frac{\mathrm{d}F}{\mathrm{d}\psi}, \tag{C6}$$

can be written in the ML coordinate system as

$$\frac{R}{(1 + \rho/R_c)} \left[ \frac{\partial}{\partial l_p} \left( \frac{(1 + \rho/R_c)}{R} \frac{\partial \psi}{\partial l_p} \right) + \frac{\partial}{\partial \rho} \left( \frac{(1 + \rho/R_c)}{R} \frac{\partial \psi}{\partial \rho} \right) \right] = -R^2 \frac{\mathrm{d}p}{\mathrm{d}\psi} - F \frac{\mathrm{d}F}{\mathrm{d}\psi}. \tag{C7}$$

To obtain the local dependence of $\psi$ on various gradients like $\mathrm{d}F/\mathrm{d}\psi$ and $\mathrm{d}p/\mathrm{d}\psi$, we write $\psi$ as an asymptotic series in terms of the normalized radial distance $\rho$

$$\psi = \psi_0 + \rho \psi_1(l_p) + \rho^2 \psi_2(l_p) + O(\rho^3), \tag{C8}$$

and define

$$\psi_1 = \lim_{\rho \to 0} \left( \frac{\psi - \psi_0}{\rho} \right) = -R_s B_{ps}, \quad \psi_1 < 0, \; B_{ps} > 0, \tag{C9}$$

where $B_{ps}$ is the on-surface poloidal magnetic field. Another way to write the above relation is to say $\nabla \psi|_{\rho=0} = \psi_1 \nabla \rho$. Using this asymptotic expansion, we can also write the following Taylor series expansions:

$$\left. \begin{aligned}
F(\psi) &= F(\psi_0) + \frac{\psi - \psi_0}{1!} \frac{\mathrm{d}F}{\mathrm{d}\psi}\bigg|_{\psi_0} + \cdots = F(\psi_0) - \rho R_s B_{ps} \frac{\mathrm{d}F}{\mathrm{d}\psi}\bigg|_{\psi_0} + \cdots, \\
F'(\psi) &= F'(\psi_0) + \frac{\psi - \psi_0}{1!} \frac{\mathrm{d}F'}{\mathrm{d}\psi}\bigg|_{\psi_0} + \cdots = F'(\psi_0) - \rho R_s B_{ps} \frac{\mathrm{d}F'}{\mathrm{d}\psi}\bigg|_{\psi_0} + \cdots, \\
p(\psi) &= p(\psi_0) + \frac{\psi - \psi_0}{1!} \frac{\mathrm{d}p}{\mathrm{d}\psi}\bigg|_{\psi_0} + \cdots = p(\psi_0) - \rho R_s B_{ps} \frac{\mathrm{d}p}{\mathrm{d}\psi}\bigg|_{\psi_0} + \cdots, \\
q(\psi) &= q(\psi_0) + \frac{\psi - \psi_0}{1!} \frac{\mathrm{d}q}{\mathrm{d}\psi}\bigg|_{\psi_0} + \cdots = q(\psi_0) - \rho R_s B_{ps} \frac{\mathrm{d}q}{\mathrm{d}\psi}\bigg|_{\psi_0} + \cdots,
\end{aligned} \right\} \tag{C10}$$

where the prime denotes a derivative with respect to $\psi$. After substituting the Taylor series expansions into the local Grad–Shafranov equation (C7), we get

$$\psi_2 = -\frac{1}{2} \left[ R_s B_{ps} \left( \frac{\sin(u)}{R_s} - \frac{1}{R_c} \right) + R_s^2 p'(\psi_0) + F(\psi_0) F'(\psi_0) \right]. \tag{C11}$$

Next, we expand the relation (2.2) about a flux surface to get

$$\begin{aligned}
\frac{\mathrm{d}q}{\mathrm{d}\psi} = {}& F' \left( \frac{q}{F} + \frac{qF}{2\pi} \oint \frac{1}{(R_s B_{ps})^2} \, \mathrm{d}\theta \right) + \frac{p'q}{2\pi} \oint \frac{\mathrm{d}\theta}{B_{ps}^2} \\
& + \frac{q}{2\pi} \oint \frac{2 \, \mathrm{d}\theta}{R_s B_{ps}} \left( \frac{\sin(u)}{R_s} - \frac{1}{R_c} \right).
\end{aligned} \tag{C12}$$

This gives us an algebraic equation defining $q'$ in terms of $F'$ and $p'$

$$\frac{1}{q}\frac{\mathrm{d}q}{\mathrm{d}\psi} = F'\left(\frac{1}{F} + \frac{F}{2\pi}\oint \mathrm{d}\theta \frac{1}{(R_s B_{ps})^2}\right) + \frac{p'}{2\pi}\oint \frac{\mathrm{d}\theta}{B_{ps}^2}$$
$$+ \frac{1}{2\pi}\oint \frac{2\,\mathrm{d}\theta}{R_s B_p s}\left(\frac{\sin(u)}{R_s} - \frac{1}{R_c}\right), \tag{C13}$$

written more compactly as

$$\frac{1}{q}\frac{\mathrm{d}q}{\mathrm{d}\psi} = F'a_{s,\mathrm{full}} + p'b_{s,\mathrm{full}} + c_{s,\mathrm{full}}, \tag{C14}$$

where $a_{s,\mathrm{full}}$, $b_{s,\mathrm{full}}$ and $c_{s,\mathrm{full}}$ are three constants obtained from doing the respective integrals in (C13). Using the ML coordinates, we can also expand the magnetic field strength around a flux surface

$$B^2 = \frac{F^2}{R^2} + \left(\frac{1}{R}\frac{\mathrm{d}\psi}{\mathrm{d}\rho}\right)^2,$$
$$= B_s^2\left[1 + \frac{2\rho}{B_s^2}\left(-\frac{B_{ps}^2}{R_c} + R_s B_{ps}p' - \frac{F^2}{R_s^3}\sin(u)\right)\right], \tag{C15}$$

which gives us the local, radial gradient of the magnetic field

$$\frac{\partial B}{\partial \rho} = \frac{1}{B_s}\left(-\frac{B_{ps}^2}{R_c} + R_s B_{ps}p' - \frac{F^2}{R_s^3}\sin(u)\right). \tag{C16}$$

To obtain all the geometric coefficients, we also need various gradients of the field-line label $\alpha$. To that end, we can write the field line label in ML coordinates as

$$\alpha = \phi + S(\rho, l_p) = \phi - q\theta, \tag{C17}$$

and find $S = S(\rho, l_p)$ by solving the equation

$$\boldsymbol{B} \cdot \nabla \alpha = 0. \tag{C18}$$

To solve (C18), we write $S(\rho, l_p)$ as an asymptotic series in $\rho$

$$S = S_0(l_p) + \rho S_1(l_p) + O(\rho^2), \tag{C19}$$

and (C18) becomes

$$\frac{F}{R^2} + \frac{1}{R(1 + \rho/R_c)}\frac{\partial \psi}{\partial \rho}\frac{\partial \alpha}{\partial l_p} - \frac{1}{R(1 + \rho/R_c)}\frac{\partial \psi}{\partial l_p}\frac{\partial \alpha}{\partial \rho} = 0. \tag{C20}$$

The lowest-order solution yields

$$S_0 = \int \mathrm{d}l_p \frac{F(\psi_0)}{R_s^2 B_{ps}} + f(\rho). \tag{C21}$$

For axisymmetric equilibria, all the field lines are identical which means we can choose $f(\rho) = 0$ without loss of generality. The next-order solution gives us

$$S_1 = -R_s B_{ps} \left[ F' \left( \frac{q\theta}{F} + F \int_0^\theta d\theta \frac{q}{(R_s B_{ps})^2} \right) \right.$$
$$\left. + p' \int_0^\theta d\theta \frac{q}{B_{ps}^2} + \int_0^\theta d\theta \frac{2q}{R_s B_{ps}} \left( \frac{\sin(u)}{R_s} - \frac{1}{R_c} \right) \right], \qquad (C22)$$

$$\frac{\partial \alpha}{\partial \rho} = S_1 = -R_s B_{ps} (F' a_s + p' b_s + c_s). \qquad (C23)$$

This completely defines the quantity $\nabla \alpha$. Using (C14), (C16), (C23) we can calculate all the geometric coefficients[13] needed for a local stability analysis. As an example, we obtain an analytical formula for the normalized local magnetic shear along the field line in a flux surface

$$\nu = -\boldsymbol{B} \cdot \nabla \left( \frac{\nabla \alpha \cdot \nabla \psi}{|\nabla \psi|^2} \right). \qquad (C24)$$

Using the following equation:

$$\boldsymbol{B} \cdot \nabla \left( \frac{\nabla \alpha \cdot \nabla \psi}{|\nabla \psi|^2} \right) = (\boldsymbol{B} \cdot \nabla \theta) \frac{\partial}{\partial \theta} \left( \frac{d\rho}{d\psi} \frac{\partial \alpha}{\partial \rho} \right), \qquad (C25)$$

we obtain the local shear

$$\nu = -\frac{F}{qR^2} \left[ \left( \frac{qF'}{F} + F'F \frac{q}{(R_s B_{ps})^2} \right) + \frac{qp'}{B_{ps}^2} + \frac{2q}{R_s B_{ps}} \left( \frac{\sin(u)}{R_s} - \frac{1}{R_c} \right) \right]. \qquad (C26)$$

One can verify that $dq/d\psi = \int_0^{2\pi} d\theta / (\boldsymbol{B} \cdot \nabla \theta) \nu$.

As another example, we calculate the geometric factor in the curvature drift

$$\tilde{\omega}_\kappa = \frac{1}{B^3} \boldsymbol{b} \times (\boldsymbol{b} \cdot \nabla \boldsymbol{b}) \cdot \nabla \alpha. \qquad (C27)$$

After using (2.5), (2.1)

$$\tilde{\omega}_\kappa = \frac{1}{B^2} \boldsymbol{b} \times \nabla (2\mu_0 p + B^2) \cdot \nabla \alpha, \qquad (C28)$$

and writing all the terms in the ML coordinate system,

$$\tilde{\omega}_\kappa = -\frac{1}{B^2} \left[ \left( \frac{d(2\mu_0 p)}{d\psi} + \frac{\partial B^2}{\partial \psi} \right) \right] + \frac{1}{B^3} \frac{F}{R} \frac{\partial \alpha}{\partial \rho} \frac{\partial B}{\partial l_p}, \qquad (C29)$$

where the radial derivatives are calculated using (C16) and (C23) analytically and $\partial B / \partial l_p$ are calculated numerically using a finite-difference scheme.

---

[13]For up–down asymmetric equilibria the lower limit in all the integrals should be some non-zero value $\theta_{\text{low}}$. To include the effect of $\theta_0$, change the lower limit of integration in (C23) from $\theta_{\text{low}}$ to $\theta_{\text{low}} + \theta_0$.

### C.3. *Variation of a local axisymmetric equilibrium*

After redefining $\rho = \sqrt{\chi/\chi_{\text{LCFS}}}$, (C14) can be written as

$$\frac{\hat{s}}{\rho} \equiv \frac{1}{q}\frac{\mathrm{d}q}{\mathrm{d}\rho} = \frac{\mathrm{d}F}{\mathrm{d}\rho}a_{s,\text{full}} + \frac{\mathrm{d}p}{\mathrm{d}\rho}b_{s,\text{full}} + c_{s,\text{full}}, \tag{C30}$$

where $a_{s,\text{full}}, b_{s,\text{full}}, c_{s,\text{full}}$ are constants. This equation implies that on a given surface, we can vary the pressure gradient $\mathrm{d}p/\mathrm{d}\rho$ and the shear $\hat{s}$ of a local equilibrium independently by a finite amount as long as we adjust $\mathrm{d}F/\mathrm{d}\rho$ such that the (C30) is satisfied. Once $\mathrm{d}p/\mathrm{d}\rho$, $\mathrm{d}q/\mathrm{d}\rho$, $\mathrm{d}F/\mathrm{d}\rho$, and the shape of the surface is fixed, we have fully defined a local equilibrium. Greene and Chance first used this idea to perform an $\hat{s} - \alpha_{\text{MHD}}$ analysis. We are going to use this for the ballooning and gyrokinetic stability analyses.

## Appendix D. Newcomb's criterion

Newcomb (1960), in his analysis of a diffuse screw pinch, described a method to infer the stability of a system to incompressible ideal-MHD modes. He reduced the ideal-MHD energy principle to

$$W = \frac{\pi}{2}\int_{r_1}^{r_2} \mathrm{d}r\left[f\left(\frac{\mathrm{d}\xi}{\mathrm{d}r}\right)^2 + g\xi^2\right], \tag{D1}$$

where $r$ is the distance from the centre, $\xi(r)$ is the radial perturbation and $f(r), g(r)$ are functions dependent on the equilibrium. One can write the kinetic energy associated with the perturbation as

$$T = \frac{\pi\omega^2}{2}\int_{r_1}^{r_2} \mathrm{d}r\xi^2. \tag{D2}$$

Combining the potential and the kinetic energy, we can write the Lagrangian $L = T - U$ and get the Euler–Lagrange equation corresponding to $\delta L = 0$

$$(f\xi')' - g\xi = \omega^2\xi. \tag{D3}$$

This equation a self-adjoint, second-order, eigenvalue ordinary differential equation (ODE). In his paper, Newcomb explored the marginally stable ODE,

$$(f\xi')' - g\xi = 0. \tag{D4}$$

For the marginally stable equation of this form, Newcomb's theorem and the associated corollary is given below:

THEOREM D.1. *If $r_1$ and $r_2$ are non-singular points of the same independent sub-interval, and if the non-trivial Euler–Lagrange solutions that vanish at $r_1$ also vanish at some point $r_0$ between $r_1$ and $r_2$, then for any Euler–Lagrange solution $\xi_0(r)$ there exist functions $\xi(r)$ with the same boundary values and with $W(r_1, r_2; \xi) < W(r_1, r_2; \xi_0)$*

COROLLARY D.2. *There exists a $\xi(r)$ that makes $W(r_1, r_2; \xi)$ negative and satisfies the boundary conditions $\xi(r_1) = \xi(r_2) = 0$*

This means that upon integrating equation (D4) with a test function $\xi$, such that $\xi(r_1) = 0$, if $\xi$ crosses the zero line at any other point, then there must exist an eigenfunction $\tilde{\xi}$ satisfying (D3) such that $W < 0$, implying that $\omega^2 < 0$. In other words, the system will have a growing eigenvalue and will become unstable.

Even though Newcomb derived this theorem for an ODE that is integrated in the radial direction, the principle can be extended to any second-order, self-adjoint, eigenvalue ODE. Hence, we can use it here for ideal ballooning, (3.3).

## Appendix E. Electromagnetic eigenfunctions at $\beta \sim 1$

In this appendix, we present two sets of eigenfunctions from the electromagnetic, negative-triangularity, inner-core, high-$\beta$ growth rate spectrum shown in figure 22(*c*).

REFERENCES

ABEL, I.G. & COWLEY, S.C. 2013 Multiscale gyrokinetics for rotating tokamak plasmas II: reduced models for electron dynamics. *New J. Phys.* **15**, 023041.

ABEL, I.G., PLUNK, G.G., WANG, E., BARNES, M., COWLEY, S.C., DORLAND, W. & SCHEKOCHIHIN, A.A. 2013 Multiscale gyrokinetics for rotating tokamak plasmas: fluctuations, transport and energy flows. *Rep. Prog. Phys.* **76**, 116201.

ADAM, J.C., TANG, W.M. & RUTHERFORD, P.H. 1976 Destabilization of the trapped-electron mode by magnetic curvature drift resonances. *Phys. Fluids* **19**, 561.

ANTONSEN, T.M. JR., DRAKE, J.F., GUZDAR, P.N., HASSAM, A.B., LAU, Y.T., LIU, C.S. & NOVAKOVSKII, S.V. 1996 Physical mechanism of enhanced stability from negative shear in tokamaks: implications for edge transport and the L-H transition. *Phys. Plasmas* **3**, 2221.

ANTONSEN, T.M. JR. & LANE, B. 1980 Kinetic equations for low frequency instabilities in inhomogeneous plasmas. *Phys. Fluids* **23**, 1205.

APPLEGATE, D.J., ROACH, C.M., CONNOR, J.W., COWLEY, S.C., DORLAND, W., HASTIE, R.J. & JOINER, N. 2007 Micro-tearing modes in the mega ampere spherical tokamak. *Plasma Phys. Control. Fusion* **49**, 1113.

BEER, M.A., COWLEY, S.C. & HAMMETT, G.W. 1995 Field-aligned coordinates for nonlinear simulations of tokamak turbulence. *Phys. Plasmas* **2**, 2687.

BELLI, E.A. & CANDY, J. 2010 Fully electromagnetic gyrokinetic eigenmode analysis of high-beta shaped plasmas. *Phys. Plasmas* **17** (11), 112314.

BERNSTEIN, I.B., FRIEMAN, E.A., KRUSKAL, M.D. & KULSRUD, R.M. 1958 An energy principle for hydromagnetic stability problems. *Proc. R. Soc.* A **244**, 17.

BISHOP, C.M. 1985 Construction of local axisymmetric MHD equilibria. *Tech. Rep.* UKAEA Culham Lab.

CANDY, J. & WALTZ, R.E. 2003*a* An Eulerian gyrokinetic-Maxwell solver. *J. Comput. Phys.* **186**, 545.

CANDY, J. & WALTZ, R.E. 2003*b* An Eulerian gyrokinetic-Maxwell solver. *J. Comput. Phys.* **186**, 545.

CATTO, P.J. & TSANG, K.T. 1977 Linearized gyrokinetic equation with collisions. *Phys. Fluids* **20**, 396.

CHANCE, M.S., JARDIN, S.C., KESSEL, C., MANICKAM, J., MONTICELLO, D., PENG, Y.K.M., HOLMES, J.A., STRICKLER, D.J., WHITSON, J.C., GLASSER, A.H., *et al.* 1990 Ideal MHD stability of very high beta tokamaks. *Tech. Rep.* Princeton University, Plasma Physics Lab.

CONNOR, J.W., HASTIE, R.J. & MARTIN, T.J. 1983 Effect of pressure gradients on the bounce-averaged particle drifts in a tokamak. *Nucl. Fusion* **23**, 1702.

CONNOR, J.W., HASTIE, R.J. & TAYLOR, J.B. 1978 Shear, periodicity, and plasma ballooning modes. *Phys. Rev. Lett.* **40**, 396.

CONNOR, J.W., HASTIE, R.J. & TAYLOR, J.B. 1979 High mode number stability of an axisymmetric toroidal plasma. *Proc. R. Soc. Lond. Ser.* A **365**, 1.

COWLEY, S.C., KULSRUD, R.M. & SUDAN, R. 1991 Considerations of ion-temperature-gradient-driven turbulence. *Phys. Fluids* B **3**, 2767.

CREELY, A.J., HOWARD, N.T., RODRIGUEZ-FERNANDEZ, P., CAO, N., HUBBARD, A.E., HUGHES, J.W., RICE, J.E., WHITE, A.E., CANDY, J., STAEBLER, G.M., *et al.* 2017 Validation of nonlinear gyrokinetic simulations of L-and I-mode plasmas on Alcator C-Mod. *Phys. Plasmas* **24**, 056104.

DAVIES, R., DICKINSON, D. & WILSON, H.R. 2022 Kinetic ballooning modes as a constraint on plasma triangularity in commercial spherical tokamaks. *Plasma Phys. Control. Fusion* **10**, 105001.

DEWAR, R.L. & GLASSER, A.H. 1983 Ballooning mode spectrum in general toroidal systems. *Phys. Fluids* **26**, 3038.

D'HAESELEER, W.D., HITCHON, W.N.G., CALLEN, J.D. & SHOHET, J.L. 2012 *Flux Coordinates and Magnetic Field Structure: A Guide to a Fundamental Tool of Plasma Theory*. Springer Science & Business Media.

DICKINSON, D., ROACH, C.M., CASSON, F.J., KIRK, A., SAARELMA, S. & SCANNELL, R. 2013 Microtearing modes and the pedestal. In *40th EPS Conference on Plasma Physics*. European Physical Society.

DORLAND, W., JENKO, F., KOTSCHENREUTHER, M. & ROGERS, B.N. 2000 Electron temperature gradient turbulence. *Phys. Rev. Lett.* **85**, 5579.

FEDERICI, G., KEMP, R., WARD, D., BACHMANN, C., FRANKE, T., GONZALEZ, S., LOWRY, C., GADOMSKA, M., HARMAN, J., MESZAROS, B., MORLOCK, C., ROMANELLI, F. & WENNINGER, R. 2014 Overview of EU DEMO design and R&D activities. *Fusion Engng Des.* **89**, 882.

FREIDBERG, J.P. 2014 *Ideal MHD*. Cambridge University Press.

FRIEMAN, E.A. & CHEN, L. 1982 Nonlinear gyrokinetic equations for low-frequency electromagnetic waves in general plasma equilibria. *Phys. Fluids* **25**, 502.

GATES, D.A. & NSTX NATIONAL RESEARCH TEAM 2003 High-$\beta$, long-pulse, bootstrap-sustained scenarios on the National Spherical Torus Experiment (NSTX). *Phys. Plasmas* **10**, 1659.

GRAD, H. & RUBIN, H. 1958 *Proceedings of the Second United Nations International Conference on the Peaceful uses of Atomic Energy*, p. 400. UN.

GREENE, J.M. & CHANCE, M.S. 1981 The second region of stability against ballooning modes. *Nucl. Fusion* **21**, 453.

GUTTENFELDER, W., CANDY, J., KAYE, S.M., NEVINS, W.M., WANG, E., BELL, R.E., HAMMETT, G.W., LEBLANC, B.P., MIKKELSEN, D.R. & YUH, H. 2011 Electromagnetic transport from microtearing mode turbulence. *Phys. Rev. Lett.* **106**, 155004.

HIGHCOCK, E.G. 2012 The zero turbulence manifold in fusion plasmas. PhD thesis, Oxford University.

HIROSE, A. 2000 On finite $\beta$ stabilization of the toroidal ion temperature gradient mode. *Phys. Plasmas* **7**, 433.

HIRSHMAN, S.P. & WHITSON, J.C. 1983 Steepest-descent moment method for three-dimensional magnetohydrodynamic equilibria. *Phys. Fluids* **26**, 3553.

HSU, S.C., ARTUN, M. & COWLEY, S.C. 1996 Calculation and interpretation of analytic high-beta poloidal equilibria in finite aspect ratio tokamaks. *Phys. Plasmas* **3**, 266.

HURRICANE, O.A., CHANDRAN, B.D.G. & COWLEY, S.C. 2000 Internal kink stability of large aspect ratio high-$\beta$ tokamaks. *Phys. Plasmas* **7**, 4043.

JARMÉN, A., MALINOV, P. & NORDMAN, H. 1998 ITG modes with finite-$\beta$ effects and the upper $\eta_i$ stability regime. *Plasma Phys. Control. Fusion* **40**, 2041.

JENKO, F. & DORLAND, W. 2001 Nonlinear electromagnetic gyrokinetic simulations of tokamak plasmas. *Plasma Phys. Control. Fusion* **43**, A141.

JOINER, N. & HIROSE, A. 2007 Effects of magnetosonic perturbations on electron temperature gradient driven modes and the stability of skin depth sized electron ballooning modes. *Phys. Plasmas* **14**, 112111.

KIM, J.Y. & HORTON, W. 1991 Electromagnetic effect on the toroidal electron temperature gradient mode. *Phys. Fluids* B*: Plasma Phys.* **3**, 3194–3197.

KOTSCHENREUTHER, M., DORLAND, W., BEER, M.A. & HAMMETT, G.W. 1995*a* Quantitative predictions of tokamak energy confinement from first-principles simulations with kinetic effects. *Phys. Plasmas* **2**, 2381.

KOTSCHENREUTHER, M., LIU, X., HATCH, D.R., MAHAJAN, S., ZHENG, L., DIALLO, A., GROEBNER, R., HILLESHEIM, J.C., MAGGI, C.F., GIROUD, C., *et al.* 2019 Gyrokinetic analysis and simulation of pedestals to identify the culprits for energy losses using 'fingerprints'. *Nucl. Fusion* **59**, 096001.

KOTSCHENREUTHER, M., REWOLDT, G.W. & TANG, W.M. 1995*b* Comparison of initial value and eigenvalue codes for kinetic toroidal plasma instabilities. *Comput. Phys. Commun.* **88**, 128.

KRUSKAL, M.D. & KULSRUD, R.M. 1958 Equilibrium of a magnetically confined plasma in a toroid. *Phys. Fluids* **1**, 265.

LANDREMAN, M., ANTONSEN, T.M. JR. & DORLAND, W. 2015 Universal instability for wavelengths below the ion larmor scale. *Phys. Rev. Lett.* **114**, 095003.

MENARD, J.E., GRIERSON, B.A., BROWN, T.G., RANA, C., ZHAI, Y., POLI, F.M., MAINGI, R., GUTTENFELDER, W. & SNYDER, P.B. 2022 Fusion pilot plant performance and the role of a sustained high power density tokamak. *Nucl. Fusion* **23**, 036026.

MERCIER, C. & LUC, H. 1974 Lectures in plasma physics. *Tech. Rep.* Commission of the European Communities.

MILLER, R.L., CHU, M.S., GREENE, J.M., LIN-LIU, Y.R. & WALTZ, R.E. 1998 Noncircular, finite aspect ratio, local equilibrium model. *Phys. Plasmas* **5**, 973.

NEWCOMB, W.A. 1960 Hydromagnetic stability of a diffuse linear pinch. *Ann. Phys.* **10**, 232.

PATEL, B.S., DICKINSON, D., ROACH, C.M. & WILSON, H.R. 2021 Linear gyrokinetic stability of a high $\beta$ non-inductive spherical tokamak. *Nucl. Fusion* **62**, 016009.

ROACH, C.M., CONNOR, J.W. & JANJUA, S. 1995 Trapped particle precession in advanced tokamaks. *Plasma Phys. Control. Fusion* **37** (6), 679.

SANCHEZ, R., HIRSHMAN, S.P., WHITSON, J.C. & WARE, A.S. 2000 COBRA: an optimized code for fast analysis of ideal ballooning stability of three-dimensional magnetic equilibria. *J. Comput. Phys.* **161**, 576.

SHAFRANOV, V.D. 1957 On equilibrium magnetohydrodynamic configurations. *Zh. Eksp. Teor. Fiz.* **33**, 710.

SHIMADA, M., CAMPBELL, D.J., MUKHOVATOV, V., FUJIWARA, M., KIRNEVA, N., LACKNER, K., NAGAMI, M., PUSTOVITOV, V.D., UCKAN, N. & WESLEY, J. 2007 Progress in the ITER physics basis chapter 1: overview and summary. *Nucl. Fusion* **47**, S1.

SYKES, A., AKERS, R.J., APPEL, L.C., CAROLAN, P.G., CONNOR, J.W., CONWAY, N.J., COUNSELL, G.F., DNESTROVSKIJ, A., DNESTROVSKIJ, Y.N., GRYAZNEVICH, M., *et al.* 2000 H-mode operation in the START spherical tokamak. *Phys. Rev. Lett.* **84**, 495.

UCHIDA, M., SEN, S., FUKUYAMA, A. & MCCARTHY, D.R. 2003 Stability of the ion-temperature-gradient-driven mode with negative magnetic shear. *Phys. Plasmas* **10**, 4758.

WHITE, A.E., HOWARD, N.T., GREENWALD, M., REINKE, M.L., SUNG, C., BAEK, S., BARNES, M., CANDY, J., DOMINGUEZ, A., ERNST, D., *et al.* 2013 Multi-channel transport experiments at Alcator C-Mod and comparison with gyrokinetic simulations. *Phys. Plasmas* **20**, 056106.

WILSON, H.R., AHN, J.W., AKERS, R.J., APPLEGATE, D., CAIRNS, R.A., CHRISTIANSEN, J.P., CONNOR, J.W., COUNSELL, G., DNESTROVSKIJ, A., DORLAND, W.D., *et al.* 2004 Integrated plasma physics modelling for the culham steady state spherical tokamak fusion power plant. *Nucl. Fusion* **44** (8), 917.

ZHU, B., FRANCISQUEZ, M., ROGERS, B.N. & XU, X.-Q. 2020 Generalized slab universal instability and its appearance in pair plasma. *Phys. Plasmas* **27**, 102104.